EUROPEAN ORGANIZATION FOR NUCLEAR RESEARCH (CERN)

CERN-EP-2022-172
2022/08/26

CMS-TOP-21-003

Search for new physics using effective field theory in 13 TeV pp collision events that contain a top quark pair and a boosted Z or Higgs boson

The CMS Collaboration

Abstract

A data sample containing top quark pairs ($\mathrm{t\bar{t}}$) produced in association with a Lorentz-boosted Z or Higgs boson is used to search for signs of new physics using effective field theory. The data correspond to an integrated luminosity of 138 fb^{-1} of proton-proton collisions produced at a center-of-mass energy of 13 TeV at the LHC and collected by the CMS experiment. Selected events contain a single lepton and hadronic jets, including two identified with the decay of bottom quarks, plus an additional large-radius jet with high transverse momentum identified as a Z or Higgs boson decaying to a bottom quark pair. Machine learning techniques are employed to discriminate between $\mathrm{t\bar{t}Z}$ or $\mathrm{t\bar{t}H}$ events and events from background processes, which are dominated by $\mathrm{t\bar{t}}$ + jets production. No indications of new physics are observed. The signal strengths of boosted $\mathrm{t\bar{t}Z}$ and $\mathrm{t\bar{t}H}$ production are measured, and upper limits are placed on the $\mathrm{t\bar{t}Z}$ and $\mathrm{t\bar{t}H}$ differential cross sections as functions of the Z or Higgs boson transverse momentum. The effects of new physics are probed using a framework in which the standard model is considered to be the low-energy effective field theory of a higher energy scale theory. Eight possible dimension-six operators are added to the standard model Lagrangian and their corresponding coefficients are constrained via fits to the data.

Submitted to Physical Review D

1 Introduction

The standard model (SM) of particle physics successfully describes a vast range of subatomic phenomena with outstanding precision. However, it cannot explain the existence of dark matter [1–3] and faces other difficulties, such as the fine-tuning or hierarchy problem [4, 5]. This indicates that the SM is incomplete and may be only a low-energy approximation, which is valid at the energies currently accessible to experiments, to a more fundamental theory. Null results from direct searches for new particles predicted by various models of physics beyond the SM (BSM) suggest that such new particles may be too massive to be produced at the CERN LHC.

The signatures of BSM physics arising from high-mass particles, which may not be directly accessible at the LHC, could appear indirectly in the form of deviations from the SM predictions for production of SM particles. All possible high-energy-scale deviations from the SM can be described at low energy scales by the SM effective field theory (EFT) [6–8]. This EFT extends the SM Lagrangian $\mathcal{L}_{\text{SM}}$ with operators $\mathcal{O}_{\text{i}}^{(d)}$ of dimension $d > 4$ and effective couplings $c_{\text{i}}^{(d)}$, known as Wilson coefficients (WCs), which are suppressed by appropriate powers of the EFT energy scale Λ, leading to an EFT Langrangian of:

$$\mathcal{L}_{\text{eff}} = \mathcal{L}_{\text{SM}} + \sum_{d,\text{i}} \frac{c_{\text{i}}^{(d)}}{\Lambda^{d-4}} \mathcal{O}_{\text{i}}^{(d)}.$$

Because of the $1/\Lambda^{d-4}$ suppression of non-SM terms, the lowest-dimension operators are the most likely to have measurable effects. Dimension-five operators produce lepton-number violation [9, 10], which is strongly constrained [11], so this analysis only considers dimension-six operators [12].

The impact of these operators may be detectable in a wide variety of experimental observables. This analysis searches for BSM effects on the production of a pair of top quarks ($\text{t}\bar{\text{t}}$) in association with a Z boson or Higgs boson (H). These processes are particularly interesting, as they provide direct access to the couplings of the top quark to the Z and Higgs bosons. Any deviations of these couplings from their SM values might imply the existence of BSM effects in the electroweak symmetry breaking mechanism, which could be probed in an EFT framework.

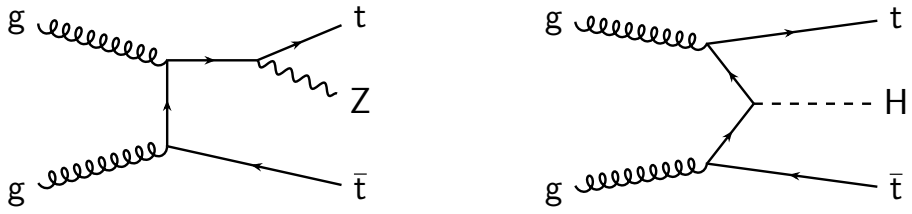

Figure 1: Examples of tree-level Feynman diagrams for the $\text{t}\bar{\text{t}}\text{Z}$ (left) and $\text{t}\bar{\text{t}}\text{H}$ (right) production processes.

The $\text{t}\bar{\text{t}}\text{Z}$ and $\text{t}\bar{\text{t}}\text{H}$ processes (Fig. 1) are challenging to measure with high precision because of their low production cross sections. However, with the large amount of data delivered by the LHC, the ATLAS and CMS Collaborations have measured the $\text{t}\bar{\text{t}}\text{Z}$ [13–16] and $\text{t}\bar{\text{t}}\text{H}$ [17–24] cross sections with a relative uncertainty of 8 and 20%, respectively. Many of these measurements, especially of $\text{t}\bar{\text{t}}\text{Z}$, have been performed in final states containing multiple charged leptons. Additionally, an extensive exploration of EFT effects in collisions producing $\text{t}\bar{\text{t}}$ in association with a W, Z, or Higgs boson has been performed by the CMS Collaboration, also in final states containing multiple charged leptons [25]. Other recent analyses have constrained the WCs

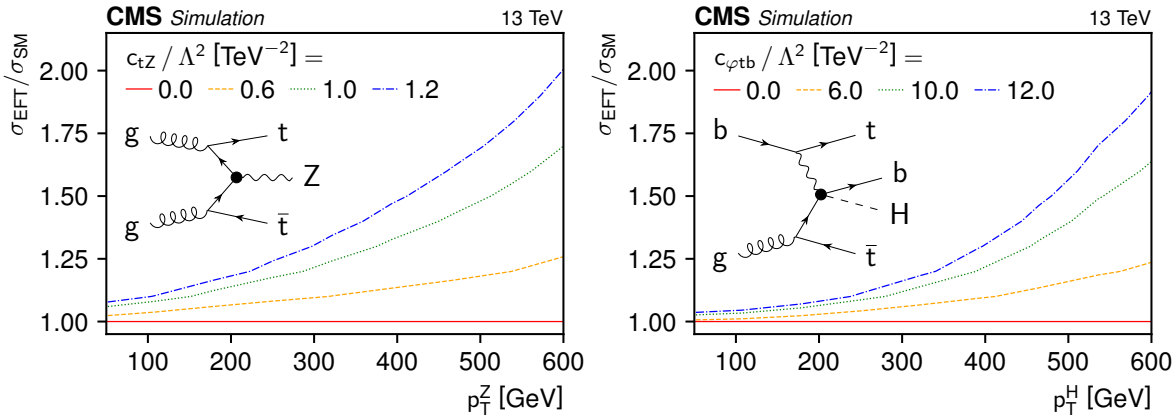

Figure 2: The $t\bar{t}Z$ (left) and $t\bar{t}H$ (right) cross sections in the SM EFT, as ratios to the corresponding SM cross sections, as functions of c_{tZ}/Λ^2 and the Z boson p_T (left), and $c_{\varphi tb}/\Lambda^2$ and the Higgs boson p_T (right), where c_{tZ} and $c_{\varphi tb}$ are the WCs for the EFT operators $O_{uB}^{(ij)}$ and $O_{\varphi ud}^{(ij)}$, respectively [7]. Example Feynman diagrams, in which the vertices affected by c_{tZ} and $c_{\varphi tb}$ are marked by a filled dot, are also displayed.

corresponding to specific EFT operators using differential and inclusive $t\bar{t}Z$ and $t\bar{t}\gamma$ measurements [13, 16, 26–28].

The fraction of $t\bar{t}Z$ and $t\bar{t}H$ events whose decay products include a single lepton is much larger than for multiple leptons, but the large background from $t\bar{t}$ produced in association with multiple jets from quantum chromodynamic (QCD) processes ($t\bar{t}$ + jets) makes measurements in single-lepton final states extremely challenging. However, at high Z or Higgs boson transverse momentum (p_T), where EFT effects are generally more pronounced, as shown in Fig. 2, we can utilize jet substructure techniques to identify $Z/H \to b\bar{b}$ decays that are reconstructed as a single merged jet, and suppress the $t\bar{t}$ + jets background. In this analysis, we probe EFT effects in $t\bar{t}Z$ and $t\bar{t}H$ events with a single lepton from the decay of one of the top quarks and a high-p_T Z or Higgs boson decaying to $b\bar{b}$.

We identify high-p_T Z or Higgs bosons decaying to $b\bar{b}$ using a large-radius jet, described below, which is identified using a machine learning technique as being consistent with the decay of a heavy boson to $b\bar{b}$. The top quark pair is identified using the combination of a single electron or muon, moderate missing transverse momentum (p_T^{miss}, defined below), at least two small-radius jets identified as originating from bottom quarks, which must be well separated from the large-radius Z or Higgs boson jet, and additional small-radius jets to account for the hadronically decaying W boson. A neural network is used to separate signal-like events from the dominant $t\bar{t}$ + jets background, and the reconstructed mass of the large-radius jet serves to distinguish $t\bar{t}Z$ and $t\bar{t}H$ events from each other, as well as from the background. A global fit to the data measures the signal strengths of the $t\bar{t}Z$ and $t\bar{t}H$ processes. We also place upper limits on the $t\bar{t}Z$ and $t\bar{t}H$ differential cross sections as functions of the p_T of the Z boson (p_T^Z) and of the Higgs boson (p_T^H), and constrain the WCs corresponding to EFT operators that most strongly affect boosted $t\bar{t}Z$ and $t\bar{t}H$ topologies.

In this paper, we briefly describe the CMS detector in Section 2 and the Monte Carlo simulation of the signals and backgrounds in Section 3. Sections 4 and 5 discuss the reconstruction of particles and selection of events, respectively, while Section 6 and Appendix A describe the neural network used to separate signal-like events from the backgrounds. In Sections 7 and 8, we detail the sources of systematic uncertainty in our measurements and present the results

of those measurements. Lastly, a summary is provided in Section 9. Tabulated results are provided in the HEPData record for this analysis [29].

2 The CMS detector

The CMS detector is a general-purpose particle detector at the LHC. It is centered on a luminous region where the LHC beams interact and is roughly symmetric under rotations around the beam direction. The inner detector is contained within a 3.8 T magnetic field produced by a 6 m internal diameter solenoid, and is composed of silicon pixel and silicon strip tracking detectors as well as a lead tungstate crystal electromagnetic calorimeter (ECAL) and a brass and scintillator hadron calorimeter. Each component of the inner detector is in turn divided into a cylindrical barrel section and two endcap sections. The magnetic flux from the solenoid is guided through a steel return yoke. Gas-ionization detectors embedded in the flux-return yoke are used to detect muons.

Events are collected using a two-tier trigger system: a hardware-based level-1 trigger [30] and a software-based high-level trigger [31]. The CMS detector is described in more detail along with the coordinate system and basic kinematic variables in Ref. [32].

3 Data and simulation samples

This analysis is performed using proton-proton (pp) collision data recorded at $\sqrt{s} = 13\,\text{TeV}$ at the LHC corresponding to an integrated luminosity of $138\,\text{fb}^{-1}$, of which 36.3, 41.5, and $59.7\,\text{fb}^{-1}$ were recorded in 2016, 2017, and 2018, respectively [33–35]. The data and simulation samples from these three years are treated separately to account for variations in the detector and LHC conditions. The data were recorded using combinations of triggers that require a single electron or muon candidate [31]. The minimum trigger p_T thresholds range from 27 to 32 GeV for electrons and from 24 to 27 GeV for muons, depending on the data-taking period.

Monte Carlo (MC) simulation is used to model signal and background events. For the $\text{t}\bar{\text{t}}\text{Z}$ and $\text{t}\bar{\text{t}}\text{H}$ signals, and for the subset of $\text{t}\bar{\text{t}}$ events containing at least one b hadron that does not originate from a top quark decay ($\text{t}\bar{\text{t}} + \text{b}\bar{\text{b}}$), two sets of MC samples are used: one set is generated at next-to-leading order (NLO) in perturbative QCD, and the other set is generated at leading order (LO) in QCD with weights corresponding to a range of WC values, representing various BSM scenarios in the SM EFT. The NLO samples (referred to as "SM samples") are used to model the expected $\text{t}\bar{\text{t}}\text{Z}$, $\text{t}\bar{\text{t}}\text{H}$, and $\text{t}\bar{\text{t}} + \text{b}\bar{\text{b}}$ contributions, while the LO samples with EFT weights ("EFT samples") are used to evaluate EFT effects relative to the SM predictions. The MADGRAPH5_aMC@NLO v2.6.0 program [36] is employed to generate the $\text{t}\bar{\text{t}}\text{Z}$ SM signal samples, while the $\text{t}\bar{\text{t}}\text{H}$ SM signal samples are generated with the POWHEG v2.0 [37–40] program. The SM $\text{t}\bar{\text{t}}\text{Z}$ signal sample is normalized to a production cross section of 0.86 pb, which is computed at NLO with next-to-next-to-leading logarithmic (NNLL) resummation in QCD [41]. Similarly, the SM $\text{t}\bar{\text{t}}\text{H}$ signal sample is normalized to a production cross section of 0.507 pb, which is computed at NLO in QCD and electroweak corrections [42] when its SM predictions are presented.

The dominant background arises from $\text{t}\bar{\text{t}}$ production. Simulated $\text{t}\bar{\text{t}}$ events are separated into three flavor categories. These categories are based on the flavor of additional jets at the particle level that do not originate from the top quark decays and that have $p_\text{T} > 20\,\text{GeV}$ and pseudorapidity $|\eta| < 2.4$: $\text{t}\bar{\text{t}} + \text{b}\bar{\text{b}}$ consists of events with at least one b hadron that does not originate from a top quark decay; $\text{t}\bar{\text{t}} + \text{c}\bar{\text{c}}$ consists of events with at least one additional jet that originates

from one or more c hadrons and no additional jets from b hadrons; and $\mathrm{t\bar{t}}$ + LF (light flavor) includes all remaining events. Within the $\mathrm{t\bar{t}} + \mathrm{b\bar{b}}$ category, the subset of events with two additional b hadrons that are sufficiently collinear to produce a single jet is denoted by $\mathrm{t\bar{t}} + 2\mathrm{b}$, and is subject to additional theoretical uncertainties. The $\mathrm{t\bar{t}} + \mathrm{b\bar{b}}$, $\mathrm{t\bar{t}} + \mathrm{c\bar{c}}$, and $\mathrm{t\bar{t}}$ + LF events are collectively referred to as $\mathrm{t\bar{t}}$ + jets events.

The $\mathrm{t\bar{t}} + \mathrm{b\bar{b}}$ events, which are the most critical background, are simulated at NLO in the four-flavor scheme (4FS). This is done using the dedicated POWHEG settings presented in Ref. [43], except that the values of the factorization and renormalization scales have been reduced by one half to approximate the effects of higher-order corrections following Ref. [44]. The $\mathrm{t\bar{t}} + \mathrm{c\bar{c}}$ and $\mathrm{t\bar{t}}$ + LF contributions are simulated using $\mathrm{t\bar{t}}$ events generated with POWHEG at NLO in the five-flavor scheme (5FS) [37–39, 45]. The top quark p_{T} spectrum in simulation is reweighted to match the prediction at next-to-next-to-leading order (NNLO) in QCD and NLO in electroweak corrections [46]. The total yield of the $\mathrm{t\bar{t}}$ events is scaled to the inclusive $\mathrm{t\bar{t}}$ cross section of 832 pb, which corresponds to the NNLO+NNLL prediction [47–53]. The fractional contributions of the $\mathrm{t\bar{t}} + \mathrm{b\bar{b}}$, $\mathrm{t\bar{t}} + \mathrm{c\bar{c}}$, and $\mathrm{t\bar{t}}$ + LF processes are set according to the 5FS $\mathrm{t\bar{t}}$ simulation, and the final $\mathrm{t\bar{t}} + \mathrm{b\bar{b}}$ yield is a free parameter in the fit to the data.

The MADGRAPH5_aMC@NLO program [36] (v2.2.2 for 2016 and v2.4.2 for 2017–2018) is used to generate the $\mathrm{t\bar{t}W}$, $\mathrm{t\bar{t}}\gamma$, $\mathrm{t\bar{t}t\bar{t}}$, s-channel single top quark, and tZq background samples at NLO in QCD. The same program is also used to generate the W + jets, Drell–Yan (DY) + jets, tHq, and tHW background samples at LO in QCD. In addition to the $\mathrm{t\bar{t}}$ samples described above, the t-channel single top quark and tW background samples are generated with the POWHEG v2.0 [37–39, 45, 54, 55] program at NLO in QCD. The Higgs boson and top quark masses are taken to be 125 and 172.5 GeV, respectively.

The simulated backgrounds other than $\mathrm{t\bar{t}}$ are also normalized to their predicted cross sections, which are taken from theoretical calculations at NLO or NNLO in QCD [41, 56–60].

All of the simulated samples use PYTHIA 8.226 (8.230) to describe parton showering and hadronization for 2016 (2017 and 2018). The samples that are simulated at NLO with MADGRAPH5_aMC@NLO use the FxFx [61] scheme for matching partons from the matrix element calculation to those from parton showers. The samples simulated at LO use the MLM [62] scheme for the same purpose. The parameters for the underlying-event description correspond to the CP5 tune [63] except for the background samples generated with MADGRAPH5_aMC@NLO for 2016, for which the CUETP8M1 [64] tune is used. The samples using the CP5 tune employ the NNPDF3.1 NNLO [65] parton distribution functions (PDFs), whereas samples using the CUETP8M1 tune employ the NNPDF3.0 LO [66] PDFs.

The simulated events are processed through a GEANT4-based [67] simulation of the CMS detector, including the effects of additional pp interactions per bunch crossing, referred to as pileup. The events are reweighted to match the estimated pileup distribution in data, based on the measured instantaneous luminosity.

3.1 Simulation of EFT samples

This analysis considers eight dimension-six EFT operators in the Warsaw basis [7] that have a large impact on the $\mathrm{t\bar{t}Z}$ and $\mathrm{t\bar{t}H}$ signal processes and minimal impacts on the background predictions. Table 1 lists the eight operators and corresponding WCs. All couplings are restricted to involve only third-generation quarks because first- and second-generation couplings have been strongly constrained by other analyses and because the $\mathrm{t\bar{t}Z}$ and $\mathrm{t\bar{t}H}$ processes are uniquely sensitive to third-generation couplings. The operators that also require their Her-

Table 1: The set of EFT operators considered in this analysis that affect the $t\bar{t}Z$ and $t\bar{t}H$ processes at order $1/\Lambda^2$. The couplings are restricted to involve only third-generation quarks. The symbol γ^μ denotes the Dirac matrices and $\sigma^{\mu\nu} \equiv i\left(\gamma^\mu\gamma^\nu - g^{\mu\nu}\right)$, where $g^{\mu\nu}$ is the metric tensor and τ^I are the Pauli matrices. The field φ is the Higgs boson doublet and $\tilde{\varphi}^j \equiv \varepsilon_{jk}\left(\varphi^k\right)^*$, where ε_{jk} is the Levi–Civita symbol and $\varepsilon_{12} = +1$. The quark doublet and the right-handed quark singlets are represented by q, u, and d, respectively. The quantities $(\varphi^\dagger i\overleftrightarrow{D}_\mu \varphi) \equiv \varphi^\dagger(iD_\mu\varphi) - (iD_\mu\varphi^\dagger)\varphi$ and $(\varphi^\dagger i\overleftrightarrow{D}^I_\mu \varphi) \equiv \varphi^\dagger\tau^I(iD_\mu\varphi) - (iD_\mu\varphi^\dagger)\tau^I\varphi$, where D_μ is the covariant derivative. The symbols $W^I_{\mu\nu}$ and $B_{\mu\nu}$ are the field strength tensors for the weak isospin and weak hypercharge gauge fields. The abbreviations $\mathcal{S}_W$ and $\mathcal{C}_W$ denote the sine and cosine of the weak mixing angle in the unitary gauge, respectively. The operators marked with the ‡ symbol also require their Hermitian conjugate in the Lagrangian.

Operator	Definition	WC
$^\ddagger O^{(ij)}_{u\varphi}$	$\bar{q}_i u_j \tilde{\varphi}\,(\varphi^\dagger\varphi)$	$c_{t\varphi} + ic^I_{t\varphi}$
$O^{(ij)}_{\varphi q}$	$(\varphi^\dagger i\overleftrightarrow{D}_\mu \varphi)(\bar{q}_i\gamma^\mu q_j)$	$c^-_{\varphi Q} + c^3_{\varphi Q}$
$O^{3(ij)}_{\varphi q}$	$(\varphi^\dagger i\overleftrightarrow{D}^I_\mu \varphi)(\bar{q}_i\gamma^\mu\tau^I q_j)$	$c^3_{\varphi Q}$
$O^{(ij)}_{\varphi u}$	$(\varphi^\dagger i\overleftrightarrow{D}_\mu \varphi)(\bar{u}_i\gamma^\mu u_j)$	$c_{\varphi t}$
$^\ddagger O^{(ij)}_{\varphi ud}$	$(\tilde{\varphi}^\dagger iD_\mu\varphi)(\bar{u}_i\gamma^\mu d_j)$	$c_{\varphi tb} + ic^I_{\varphi tb}$
$^\ddagger O^{(ij)}_{uW}$	$(\bar{q}_i\sigma^{\mu\nu}\tau^I u_j)\,\tilde{\varphi}W^I_{\mu\nu}$	$c_{tW} + ic^I_{tW}$
$^\ddagger O^{(ij)}_{dW}$	$(\bar{q}_i\sigma^{\mu\nu}\tau^I d_j)\,\varphi W^I_{\mu\nu}$	$c_{bW} + ic^I_{bW}$
$^\ddagger O^{(ij)}_{uB}$	$(\bar{q}_i\sigma^{\mu\nu} u_j)\,\tilde{\varphi}B_{\mu\nu}$	$\frac{\mathcal{C}_W}{\mathcal{S}_W}(c_{tW} + ic^I_{tW}) - \frac{1}{\mathcal{S}_W}(c_{tZ} + ic^I_{tZ})$

mitian conjugate term in the Lagrangian (marked with ‡ in Table 1) can have complex WCs; however, imaginary coefficients lead to charge-conjugation and parity violation, and are generally already constrained [12]. Therefore, following a similar strategy to that used in an earlier CMS analysis [25], only the eight real-component WCs in Table 1 are considered in this analysis.

Samples with EFT effects are generated for the $t\bar{t}Z$ and $t\bar{t}H$ signal processes and the $t\bar{t} + b\bar{b}$ background using the MADGRAPH5_aMC@NLO v2.6.5 event generator at LO and the NNPDF3.1 NNLO PDF set, following a similar approach to that outlined in Ref. [12]. The EFT effects on the decay of the top quark and the Z and Higgs bosons are expected to be negligible, and are not considered. As is done for the SM samples, the EFT samples are processed through a GEANT4-based [67] simulation of the CMS detector, and event reconstruction is performed in the same manner as for the collision data. Samples of $t\bar{t} + LF$ and $t\bar{t} + c\bar{c}$ background events are also generated with EFT effects, and no observable variations are seen for the eight operators considered. The $t\bar{t} + b\bar{b}$ sample shows a nonnegligible EFT effect when varying c_{bW}, which is accounted for in the analysis. The $t\bar{t}Z$ and $t\bar{t}H$ signal samples are generated with up to one extra parton in the final state. This improves the precision of the simulation, bringing it closer to NLO in QCD [25, 68]. The EFT effects from this approach are found to be compatible with those from the SMEFT@NLO model [69] for the dimension-six operators included in SMEFT@NLO [68].

In the EFT samples, the effects of varying the eight WCs are computed as a weighting factor for each simulated event. The weight w_{EFT} for each event is parameterized as a quadratic function of the eight WCs:

$$w_{EFT} = s_0 + \sum_i s_{1i}\frac{c_i}{\Lambda^2} + \sum_{i,j} s_{2ij}\frac{c_i}{\Lambda^2}\frac{c_j}{\Lambda^2}, \tag{1}$$

where s_0 is the weight arising only from SM processes, subscripts i and j are indices for WCs

under consideration, s_{1i} is the coefficient for the term arising from the interference between one EFT operator and the SM, and s_{2ij} is the coefficient for the term arising from interference between two EFT operators (for $i \neq j$) or for the term arising solely from one EFT operator (for $i = j$). In the SM, where all WCs are zero, w_{EFT} is equal to s_0.

4 Event reconstruction

Collisions in the CMS detector are reconstructed using the particle-flow (PF) algorithm [70]. This algorithm exploits information from every subsystem of the detector and produces candidate reconstructed objects (PF candidates) in several categories: charged and neutral hadrons, photons, electrons, and muons. The PF candidates are used, in various combinations, to reconstruct higher-level objects such as interaction vertices, hadronic jets, and the $\vec{p}_T^{\,miss}$. This section describes the reconstruction of the objects that are used in this analysis.

The $\vec{p}_T^{\,miss}$ vector, which is used to estimate the summed $\vec{p}_T$ of neutrinos in the event, is defined as the negative vector sum of the $\vec{p}_T$ of all PF candidates in the event [71]. Its magnitude is denoted by p_T^{miss}.

An interaction vertex is a point from which multiple tracks in one event originate. The primary vertex (PV) is taken to be the interaction vertex corresponding to the hardest scattering in the event, evaluated using tracking information alone, as described in Section 9.4.1 of Ref. [72]. All selected objects in this analysis must be associated with the PV.

Electron candidates are reconstructed and identified by combining information from the ECAL and the tracking system [73], and they are required to have $|\eta| < 2.5$ and $p_T > 30$ (35) GeV for 2016 (2017 and 2018). The variation of the electron candidate p_T requirement is related to a change in the electron trigger between 2016 and 2017. Muon candidates are reconstructed as tracks in the silicon tracking system consistent with measurements in the muon system, and associated with calorimeter deposits compatible with the muon hypothesis [74]. Muon candidates are required to have $|\eta| < 2.4$ and $p_T > 30$ GeV. Electron and muon candidates are required to be isolated from surrounding hadronic activity and to be consistent with an origin at the PV.

The electron and muon isolation requirement is based on the mini-isolation variable I_{mini}, which is defined as the scalar sum of the p_T of all charged hadron, neutral hadron, and photon PF candidates within a variably sized cone around the electron or muon candidate direction [75]. The cone radius $\Delta R = \sqrt{(\Delta\eta)^2 + (\Delta\phi)^2}$ is 10 GeV divided by the lepton p_T within the range $50 < p_T < 200$ GeV. For leptons with $p_T < 50$ GeV (>200 GeV), we use $\Delta R = 0.2$ (0.05). The mini-isolation variable is corrected for contributions from pileup using estimates of the charged and neutral pileup energy inside the cone [73, 74]. Electron and muon candidates are required to have $I_{mini}/p_T < 0.2$ and 0.1, respectively. The overall trigger efficiency, measured in a control region requiring one electron and one muon, is around 86% (87%) for events with an electron (muon) that satisfies these selection criteria.

Two types of jets, small-radius ("AK4") and large-radius ("AK8"), are used in this analysis. Both are reconstructed by clustering charged and neutral PF candidates using the anti-k_T jet finding algorithm [76, 77], with distance parameters of 0.4 and 0.8, respectively.

The AK4 jets use charged-hadron subtraction [78] for pileup mitigation and are required to have $p_T > 30$ GeV and $|\eta| < 2.4$. The AK8 jets use the pileup per particle identification algorithm [78, 79] to reduce the effects of pileup and are required to have $p_T > 200$ GeV, $|\eta| < 2.4$, and an invariant mass between 50 and 200 GeV. The invariant mass of each AK8 jet, m_{SD}, is cal-

culated using the soft-drop algorithm [80, 81] with an angular exponent $\beta = 0$ and soft cutoff threshold $z_{\text{cut}} = 0.1$. This algorithm systematically removes soft and collinear radiation from the jet. Its performance in collision data is validated in Ref. [82].

Jet quality criteria [78] are imposed to eliminate jets from spurious sources such as electronics noise. The jet energies are corrected for residual pileup effects [83] and the detector response as a function of p_{T} and η [84]. All jets are required to be separated from the selected electron or muon candidate by $\Delta R > 0.4$ or 0.8 for AK4 and AK8 jets, respectively. Selected AK4 jets may overlap spatially with selected AK8 jets, and may use the same PF candidates.

Jets originating from the hadronization of bottom quarks (b jets) are identified (b tagged) using a secondary-vertex algorithm based on a deep neural network (DEEPCSV) [85]. The "medium" working point of this algorithm is used, which provides a tagging efficiency of 68% for typical b jets from top quark decays [85]. The corresponding misidentification probability for light-flavor jets, which contain only light-flavor hadrons and originate from gluons and up, down, and strange quarks, is 1%, and for charm quark jets (c jets) it is 12% [85].

When a Z or Higgs boson is produced with a large Lorentz boost, its decay products will be collimated and may be reconstructed as a single AK8 jet. We employ a multivariate discriminant to identify AK8 jets containing the decay products from a $\mathrm{b\bar{b}}$ pair. This discriminant is based on a dedicated deep neural network algorithm, the DEEPAK8 $\mathrm{b\bar{b}}$ tagger [82], which is uncorrelated with m_{SD}. By combining the tagger output and m_{SD}, we can identify jets consistent with $\mathrm{Z} \to \mathrm{b\bar{b}}$ and $\mathrm{H} \to \mathrm{b\bar{b}}$ decays and use the m_{SD} regions away from the Z and Higgs boson masses as background-enriched control regions. The $\mathrm{b\bar{b}}$ tagger produces a score between 0 and 1. The selected AK8 jet with the largest score in each event is identified as the Z or Higgs boson candidate, provided that the score is greater than 0.8. This $\mathrm{b\bar{b}}$ tagger score requirement together with the m_{SD} requirement produces a $\mathrm{b\bar{b}}$ tagging efficiency of 65–85% for $\mathrm{Z} \to \mathrm{b\bar{b}}$ decays and 40–75% for $\mathrm{H} \to \mathrm{b\bar{b}}$ decays, depending on the p_{T} of the AK8 jet. The misidentification rate is roughly 2.5% for jets from QCD multijet events.

5 Event selection

This analysis targets $\mathrm{t\bar{t}Z}$ or $\mathrm{t\bar{t}H}$ production, where the $\mathrm{t\bar{t}}$ decay products include an electron or muon and a neutrino, plus two b quarks and two other quarks, and the Z or Higgs boson decays to a $\mathrm{b\bar{b}}$ pair. We select events containing exactly one candidate electron or muon, $p_{\text{T}}^{\text{miss}} > 20\,\text{GeV}$, five or more AK4 jets, and a Z or Higgs boson candidate AK8 jet. The electron or muon and the $p_{\text{T}}^{\text{miss}}$ are expected to arise from the leptonic decay of a W boson. At least one (and sometimes two) of the AK4 jets spatially overlap the AK8 jet because the AK4 and AK8 jet clustering algorithms run independently with no unambiguous way to distinguish AK4 and AK8 jets that share some or all of of their constituent particles. Three or four AK4 jets, corresponding to the hadrons from the $\mathrm{t\bar{t}}$ decay products, are expected to be well separated from the AK8 jet. At least two AK4 jets must be b tagged and separated from the Z or Higgs boson candidate jet by $\Delta R > 0.8$. These requirements are summarized in Table 2.

To remove events with spurious $p_{\text{T}}^{\text{miss}}$, we use the event filters described in Ref. [71]. In addition, events in which the lepton candidate and a second lepton of the same flavor but opposite charge have an invariant mass less than 12 GeV are removed from the data set to eliminate leptons from J/ψ or Υ meson decay. This requirement, in combination with the $p_{\text{T}}^{\text{miss}}$ threshold, is effective at significantly reducing the nonprompt-lepton background. The p_{T}, isolation, and identification requirements are relaxed for the second lepton, because it typically has lower momentum than the primary lepton candidate. Lastly, we remove events that contain an electron PF candidate

Table 2: Summary of the reconstructed object and event selection requirements.

Missing transverse momentum	$p_{\mathrm{T}}^{\mathrm{miss}} > 20\,\mathrm{GeV}$
=1 electron or muon	$p_{\mathrm{T}}(\mathrm{e}) > 30$ (35 GeV) in 2016 (2017 and 2018) $p_{\mathrm{T}}(\mu) > 30\,\mathrm{GeV}$ $\lvert\eta(\mathrm{e})\rvert < 2.5$, $\lvert\eta(\mu)\rvert < 2.4$ $I_{\mathrm{mini}}(\mathrm{e})/p_{\mathrm{T}}(\mathrm{e}) < 0.2$, $I_{\mathrm{mini}}(\mu)/p_{\mathrm{T}}(\mu) < 0.1$
$\geq$1 AK8 jet	$p_{\mathrm{T}} > 200\,\mathrm{GeV}$, $\lvert\eta\rvert < 2.4$ $50 < m_{\mathrm{SD}} < 200\,\mathrm{GeV}$
=1 Z or Higgs boson candidate AK8 jet	Highest $\mathrm{b\bar{b}}$ tagger score ($>$0.8)
$\geq$5 AK4 jets (may overlap AK8 jets)	$p_{\mathrm{T}} > 30\,\mathrm{GeV}$, $\lvert\eta\rvert < 2.4$
$\geq$2 b-tagged AK4 jets	Satisfy medium DEEPCSV b tag requirements ΔR(b-tagged AK4 jet, Z or Higgs boson candidate) > 0.8

with $p_{\mathrm{T}} > 20\,\mathrm{GeV}$, $-3 < \eta < -1.4$, and $-1.57 < \phi < -0.87$ during the latter part of 2018 because of a malfunction in that part of the hadron calorimeter.

6 Discrimination of signal against backgrounds

To separate boosted $\mathrm{t\bar{t}Z}$ and $\mathrm{t\bar{t}H}$ signal events from background, we use three discriminating variables: the p_{T} and m_{SD} of the reconstructed Z or Higgs boson candidate AK8 jet, and a global event neural network score. These variables allow us to define regions that are enriched in $\mathrm{t\bar{t}Z}$, regions that are enriched in $\mathrm{t\bar{t}H}$, and regions that are dominated by background but kinematically similar to the signal-dominated regions. The use of the boson candidate p_{T} allows us to place upper limits on the $\mathrm{t\bar{t}Z}$ and $\mathrm{t\bar{t}H}$ cross sections differentially as functions of $p_{\mathrm{T}}^{\mathrm{Z}}$ and $p_{\mathrm{T}}^{\mathrm{H}}$, respectively, and provides additional sensitivity to the effects of BSM physics.

6.1 Global Event Neural network

We train a deep neural network (DNN) to discriminate between simulated signal events and simulated $\mathrm{t\bar{t}}$ + jets background events. The DNN has 50 input variables, two dense hidden layers, and an output layer consisting of three output nodes. The input variables describe the kinematic properties of reconstructed events and are chosen to provide discrimination power between $\mathrm{t\bar{t}Z}$ or $\mathrm{t\bar{t}H}$ and the $\mathrm{t\bar{t}}$ + jets background, with an emphasis on discrimination against $\mathrm{t\bar{t}} + \mathrm{b\bar{b}}$ events. All of the input variables are listed in Table A.1 in Appendix A, and a subset of the input variable distributions, consisting of variables that rank high in the mutual information feature importance metric [86, 87], is shown in Fig. A.1. These distributions are used to verify that the input variables are well modeled. Correlations and nonlinear relationships among the input variables are also well understood, which we verify by comparing the expected and observed distributions of the outputs of the final hidden layer of the DNN.

The variables targeting top quark decays include the b tagger scores and jet p_{T} values, the invariant masses of sets of two or three jets, and the spatial separation between pairs of jets or between jets and leptons. The AK8 jets originating from the decays of boosted Z or Higgs bosons are identified using the $\mathrm{b\bar{b}}$ discriminant score, the number of b-tagged AK4 jets overlapping the AK8 jet, and the separations between and invariant masses of the candidate AK8 jet and various leptons and jets presumed to come from the $\mathrm{t\bar{t}}$ decay products. Global event variables, including summed p_{T}, sphericity, and aplanarity [88], are calculated using the selected lepton and AK4 jet momenta and the $\vec{p}_{\mathrm{T}}^{\,\mathrm{miss}}$. We combat overtraining of the neural network by employing a batch normalization layer [89] and a dropout layer [90], and by evaluating the

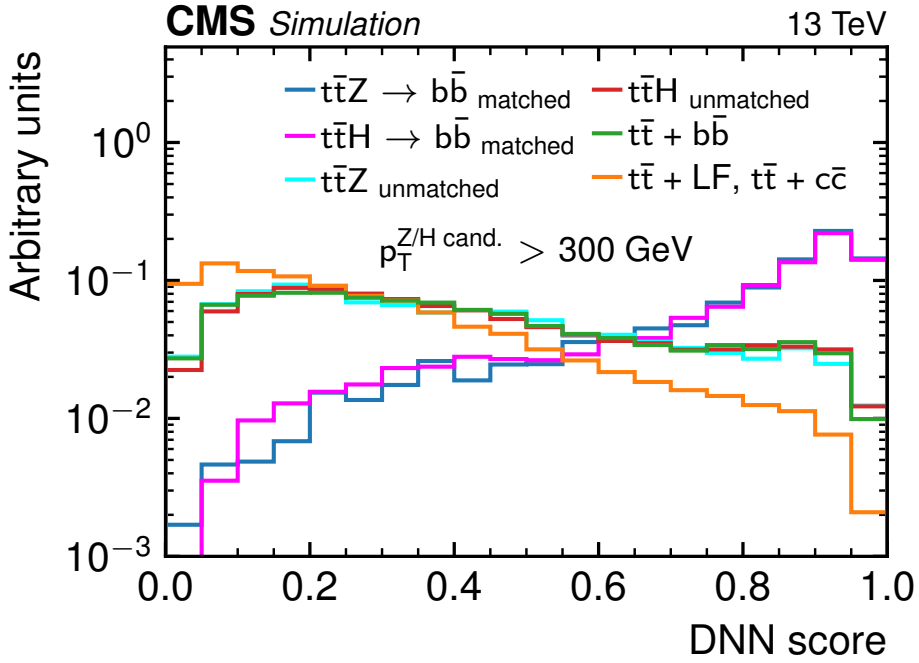

Figure 3: The simulated DNN score distributions, normalized to unit area, for well-reconstructed $t\bar{t}Z$ and $t\bar{t}H$ signal events in which the reconstructed Z or Higgs boson candidate is matched to both generator-level b quark daughters of the Z or Higgs boson; the remaining $t\bar{t}Z$ and $t\bar{t}H$ events; background events from $t\bar{t} + b\bar{b}$; and background events from $t\bar{t} + c\bar{c}$ and $t\bar{t}$ + LF. The events satisfy the baseline selection requirements described in Section 5 and contain a Z or Higgs boson candidate with $p_T > 300\,\text{GeV}$.

training with an independent validation data set, which is 60% of the size of the training data set.

This neural network is a multiclass classifier with three output nodes, each trained to identify a single class of events: $t\bar{t}Z$ and $t\bar{t}H$ signal, $t\bar{t} + b\bar{b}$ background, and $t\bar{t}$ + LF and $t\bar{t} + c\bar{c}$ background. Only well-reconstructed $t\bar{t}Z$ and $t\bar{t}H$ signal events are used in the training, i.e., the reconstructed Z or Higgs boson candidate is matched to both generator-level b quark daughters of the Z or Higgs boson with $\Delta R(\text{AK8 jet}, b) < 0.6$. The three outputs for each event are scaled so that their sum is one. The focal loss function [91] is employed to balance the relative importance of the three classes of events during training despite an imbalance in the number of simulated events in each class.

Although multiple classes are used during training, only the signal-oriented output node is used in the analysis for the purpose of distinguishing background from signal. Even though they are not directly used, the two background-oriented nodes do affect the signal-oriented output via the scaling, and their presence improves the discrimination power compared to a binary-classification neural network. Figure 3 shows the DNN output score for well-reconstructed $t\bar{t}Z$ and $t\bar{t}H$ signal events, for $t\bar{t}Z$ and $t\bar{t}H$ events that either do not contain a Z or Higgs boson decaying to $b\bar{b}$ or are not well reconstructed, for $t\bar{t} + b\bar{b}$ background events, and for $t\bar{t} + c\bar{c}$ and $t\bar{t}$ + LF background events. The distributions of well-reconstructed signal events show strong separation from those of background events, especially $t\bar{t} + c\bar{c}$ and $t\bar{t}$ + LF. All $t\bar{t}Z$ and $t\bar{t}H$ events, even those that either do not contain $Z/H \to b\bar{b}$ or are not well reconstructed, are included as signal events in the analysis, even though they are separated in Fig. 3. Because our sensitivity to BSM effects is dominated by high-p_T events, Fig. 3 only includes events with $p_T^{Z/H} > 300\,\text{GeV}$.

6.2 Analysis bins

Data collected in 2016, 2017, and 2018 are treated separately, and are divided among bins based on the p_T and m_{SD} of the reconstructed Z or Higgs boson candidate and the DNN score. The DNN score provides signal-rich and background-rich regions, enhancing the sensitivity of the analysis. The m_{SD} provides a region enriched in $t\bar{t}Z$ in the vicinity of the Z boson mass, a region enriched in $t\bar{t}H$ in the vicinity of the Higgs boson mass, and two sidebands with higher and lower m_{SD} that are kinematically similar but depleted in $t\bar{t}Z$ and $t\bar{t}H$ signal. The sensitivity to BSM effects is enhanced at high p_T, as shown in Fig. 2, so binning based on the reconstructed p_T of the boson candidate improves the resulting constraints on the WCs.

Events from each year are divided among three bins based on the p_T of the reconstructed Z or Higgs boson candidate: 200–300, 300–450, and >450 GeV, motivated by the simplified template cross section binning definition for $t\bar{t}H$ [42]. Within each p_T range, events are assigned to one of six bins based on the DNN score. The DNN score binning is unique to each p_T bin in each year, and is chosen so that the $t\bar{t}Z$ and $t\bar{t}H$ signal events are divided among six intervals bounded by 0, 5, 25, 35, 50, 70, and 100% of the total expected yield of well-reconstructed signal events, ordered from low to high DNN score.

Within each p_T and DNN score bin, the data are divided among four m_{SD} bins: 50–75, 75–105, 105–145, and 145–200 GeV. In the lowest p_T bin, the two highest mass bins are merged to $105 < m_{SD} < 200$ GeV because of low signal and background yields. Figure 4 shows the m_{SD} distributions of reconstructed Z or Higgs boson candidates in three p_T ranges for simulated signal and background events. The $75 < m_{SD} < 105$ GeV bin provides a $t\bar{t}Z$ enriched region for all candidate AK8 jet p_T values, while the $105 < m_{SD} < 145$ GeV bin is enriched in $t\bar{t}H$ for $p_T > 300$ GeV. The $t\bar{t}H$ events with $p_T < 300$ GeV do not show a clear peak in m_{SD} around the Higgs boson mass, because its decay products are less likely to be fully contained in the AK8 jet. Binning using the boson candidate p_T and m_{SD} and the DNN score results in a total of 66 bins for each data-taking year.

When setting upper limits on the differential cross sections as functions of p_T^Z and p_T^H, the $t\bar{t}Z$ and $t\bar{t}H$ simulated signal samples are each divided into four subsamples according to the p_T of the simulated Z or Higgs boson, respectively. The p_T^Z and p_T^H bins are 0–200, 200–300, 300–450, and >450 GeV. The three highest p_T bins match the candidate AK8 jet p_T bins, and are used to obtain the differential cross section results. In events that fall into the generator-level $p_T^{Z/H} < 200$ GeV bin, the Z or Higgs boson does not have sufficient boost to be reconstructed as a single AK8 jet. Therefore, the rate of those events is not treated as an unconstrained parameter, but rather is fixed to the SM expectation. For the measurement of the signal strengths of the $t\bar{t}Z$ and $t\bar{t}H$ processes with generator-level $p_T^{Z/H} > 200$ GeV, the subsample with generator-level $p_T^{Z/H} < 200$ GeV is fixed to the SM expectation, but it is unconstrained for the measurement of the WCs. Figure 5 shows the expected distribution of the candidate AK8 jet p_T in each of the three highest p_T subsamples of SM $t\bar{t}Z$ and $t\bar{t}H$ production for the subset of events that fall into the two or three highest DNN bins and have an AK8 jet mass consistent with Z or Higgs boson decay. These two-dimensional distributions serve as the folding matrices M_{ij}, which describe the relationship between the simulated and reconstructed distributions, when setting upper limits on the differential cross sections.

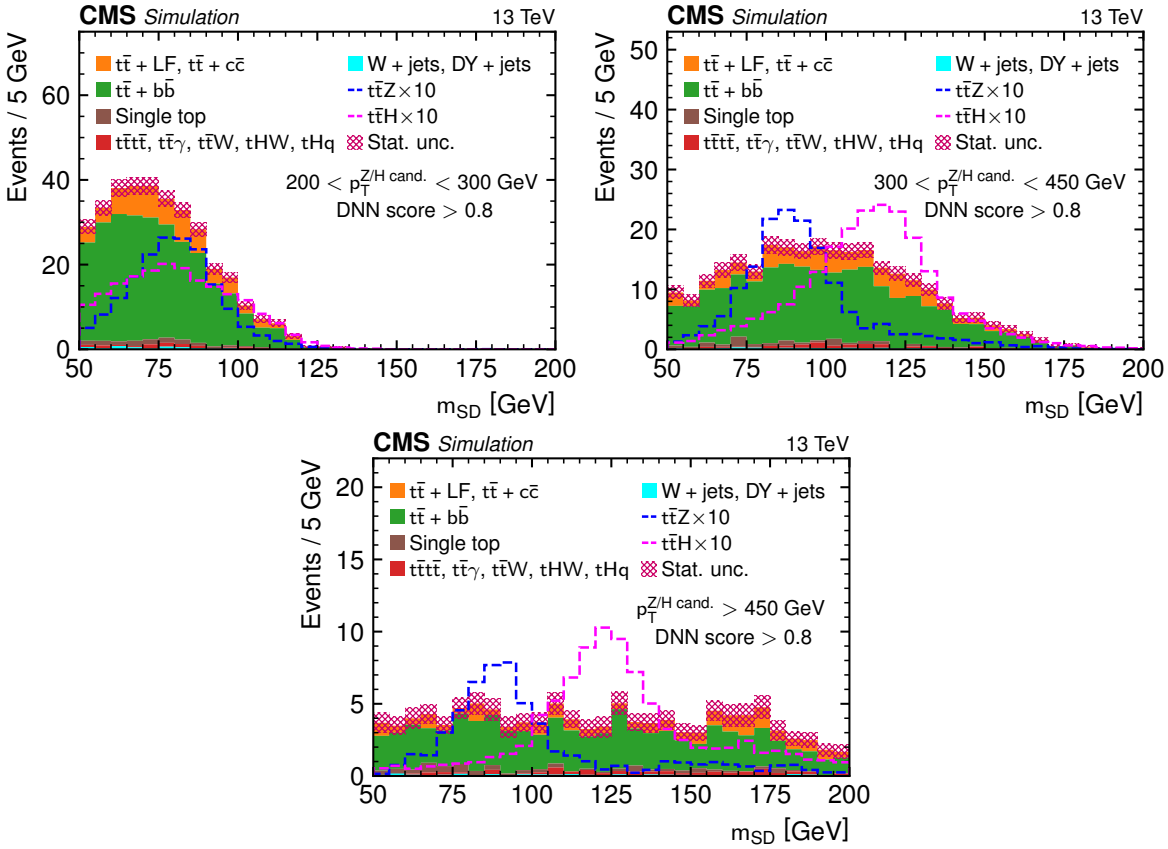

Figure 4: Soft-drop mass distributions from simulation for background (solid histograms) and signal (dashed histograms) of $Z/H \to b\bar{b}$ candidate jets in three p_T ranges: 200–300 GeV (upper left), 300–450 GeV (upper right), and >450 GeV (lower) in simulated samples with DNN score >0.8. The signal distributions represent the SM prediction scaled up by a factor of 10 for easier comparison with the backgrounds. The signal distributions include well-reconstructed $t\bar{t}Z$ and $t\bar{t}H$ events as well as $t\bar{t}Z$ and $t\bar{t}H$ events that either do not contain $Z/H \to b\bar{b}$ or are not well reconstructed. The red hatched bands correspond to the statistical uncertainty in the background.

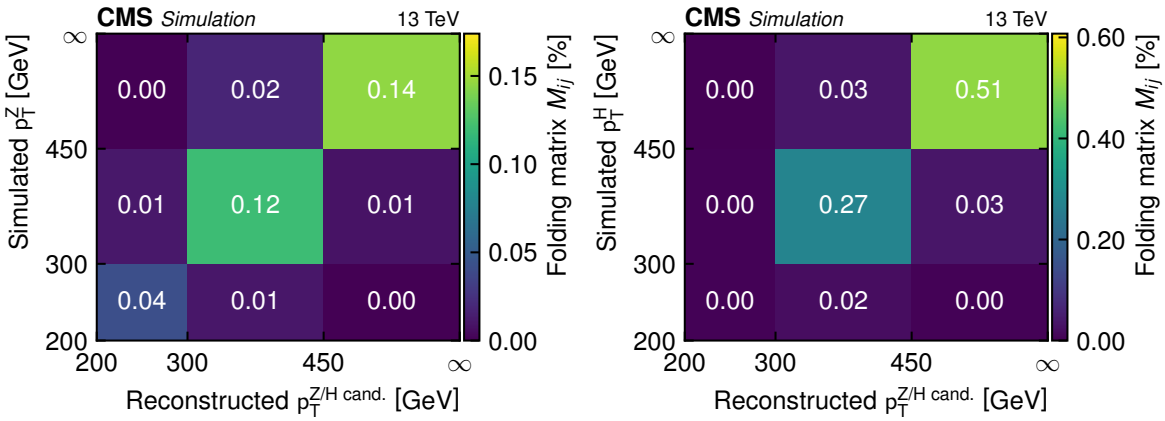

Figure 5: The percentage of simulated $t\bar{t}Z$ (left) and $t\bar{t}H$ (right) signal events that satisfy the baseline event selection requirements as well as the DNN and mass requirements in bins defined by the reconstructed AK8 jet p_T (x axis) and simulated $p_T^{Z/H}$ (y axis). The rightmost and uppermost bins are unbounded. The value of each bin is the ratio of the event yield in the bin to the total number of simulated signal events with a simulated $p_T^{Z/H}$ in the same y-axis bin, including all decay modes of the top quark, Z boson, and Higgs boson. The color scale to the right shows the meaning of the histogram colors.

7 Systematic uncertainties

The systematic uncertainties in the measurements arise from theoretical and experimental sources and may affect both the overall rates of the signals and backgrounds, as well as the shapes of the templates used in the fit to the data. The systematic uncertainties are treated as nuisance parameters in the final fit to the data. Except where otherwise noted, the nuisance parameters are given Gaussian constraints in the fit. The theoretical uncertainties are all treated as fully correlated across the entire data-taking period, while some of the experimental uncertainties are treated independently in each data-taking year and others are fully correlated.

We account for the statistical uncertainty in the simulation caused by the finite size of the simulated data sets using the approach described in Refs. [92, 93].

7.1 Theoretical uncertainties

The signal and background processes are scaled according to their expected cross sections, which are calculated at NLO or higher order as described in Section 3. The uncertainties in these cross sections arise from the choice of the renormalization (μ_R) and factorization scales (μ_F) as well as from uncertainty in the PDFs, including uncertainty in the value of the strong coupling constant α_S used in the PDFs. The scales μ_R and μ_F are varied up and down by a factor of two, and the PDFs and α_S are varied following the PDF4LHC prescription [94]. The resulting variation in the cross sections is treated as a set of nuisance parameters with log-normal constraints depending on the process and the initial state. These nuisance parameters only affect the overall yield of each process.

The choice of μ_R and μ_F scales, as well as the PDF, may also affect the simulation of the kinematic distributions of the particles in the final state. In the simulation of the matrix elements, the scales are varied up and down by a factor of two, and the PDF is varied within its uncertainties [94]. Similarly, the scales that control the amount of initial- and final-state radiation are varied up and down independently by a factor of two. Although the parton shower scale variations affect all processes, special handling is required for the $t\bar{t} + b\bar{b}$ background. Variations

in the parton shower scales affect the fraction of $\mathrm{t\bar{t}} + \mathrm{b\bar{b}}$ events within the $\mathrm{t\bar{t}}$ + jets background. The effect on the $\mathrm{t\bar{t}} + \mathrm{b\bar{b}}$ yield is calculated within the $\mathrm{t\bar{t}}$ + jets (5FS) MC sample and then propagated to the $\mathrm{t\bar{t}} + \mathrm{b\bar{b}}$ (4FS) MC sample. Because the effect of these uncertainties on the overall yields has already been accounted for, these variations only affect the acceptance or the shape of the distributions in the inclusive phase space. This is treated as a set of nuisance parameters, depending again on the process and the initial state.

For the POWHEG samples, the matching between the matrix element and parton shower simulation of the $\mathrm{t\bar{t}}$ + jets backgrounds is governed by the h_{damp} parameter. The $\mathrm{t\bar{t}}$ + jets backgrounds are simulated with $h_{\mathrm{damp}} = 1.379 m_{\mathrm{t}}$, where m_{t} is the mass of the top quark, and smaller simulated samples are produced with $h_{\mathrm{damp}} = 0.874 m_{\mathrm{t}}$ and $h_{\mathrm{damp}} = 2.305 m_{\mathrm{t}}$ to evaluate the effects of varying this parameter [63]. We treat this uncertainty as a nuisance parameter with a log-normal constraint that affects the overall yields of the $\mathrm{t\bar{t}}$ + jets backgrounds.

Any remnants of the pp collision that do not participate in the hard-scattering process are referred to as the "underlying event". The simulation is tuned to reproduce the kinematic distributions of the underlying event [63]. The effects of the residual uncertainty in the tune are evaluated in separate simulations of the $\mathrm{t\bar{t}}$ + jets backgrounds. The uncertainty in the underlying-event tune is treated as a nuisance parameter with a log-normal constraint affecting the overall yields of the $\mathrm{t\bar{t}}$ + jets backgrounds.

The cross section of the $\mathrm{t\bar{t}} + \mathrm{b\bar{b}}$ background is treated as an unconstrained nuisance parameter. Moreover, the rate of the $\mathrm{t\bar{t}} + 2\mathrm{b}$ subset of the $\mathrm{t\bar{t}} + \mathrm{b\bar{b}}$ background is varied by up to 50% because of the uncertainty in modeling the gluon fragmentation process [95].

The $\mathrm{t\bar{t}} + \mathrm{c\bar{c}}$ production cross section has been measured with an uncertainty of approximately 20% [96]. However, we assume a larger uncertainty of 50% because of the differences between the phase space studied in Ref. [96] and the phase space relevant for this study.

7.2 Experimental uncertainties

The templates in the fit are scaled to their expected yields using the integrated luminosity represented by our data set. The integrated luminosities recorded in 2016, 2017, and 2018 are measured with uncertainties of 1.2, 2.3, and 2.5%, respectively [33–35]. These measurements are mostly uncorrelated from year to year, and we treat the uncertainty in the integrated luminosity with a set of nuisance parameters with log-normal constraints representing the correlated and uncorrelated components. This does not affect the shapes of the templates, while all of the other experimental uncertainties do affect the template shapes.

The distribution of the number of pileup interactions in simulated events is reweighted to match the observed pileup distribution in data, assuming a total inelastic pp cross section of 69.2 mb [97]. This cross section is varied up and down by 4.6%, and the resulting effects on the simulation are treated as independent nuisance parameters for each year. This accounts for year-to-year variations in the differences between the interaction vertex multiplicity distribution in data and simulation.

The simulation is corrected, using p_{T}- and η-dependent scale factors, for residual differences between data and simulation in the reconstruction, identification, and isolation of the lepton, and in the trigger efficiency. The uncertainties in these scale factors are treated as independent nuisance parameters for each year. The trigger efficiency scale factor includes a correction and accompanying uncertainty component caused by a gradual drift in the timing of the inputs to the ECAL level-1 trigger in the forward region during 2016 and 2017 [30].

The jet energy scales for AK4 and AK8 jets in simulation are corrected to match data, and these corrections are varied within their uncertainties [84]. These effects are split among 11 independent subsources of uncertainty, some of which are correlated among the years. The uncertainty subsources affecting both AK4 and AK8 jets are treated as correlated. Similarly, the energy resolutions of AK4 and AK8 jets are known to be worse in data than in simulation, so the simulated jet energies are smeared to improve their agreement with data [84]. The amount of smearing is varied within the uncertainty in the required amount of smearing, and the effects of this variation are handled independently for each year. Additionally, the smearing procedure is performed independently for AK4 and for AK8 jets, so the corresponding uncertainties are uncorrelated. Corrections are also applied to the scale and resolution of m_{SD} for AK8 jets, and these corrections are varied within their uncertainties. The effects of these variations are treated as independent nuisance parameters for each year.

The performance of the DEEPCSV b tagger is slightly different in simulation than in data. We correct the simulation separately for the tagging of b jets, the tagging of c jets, and the misidentification of light-flavor jets using efficiency scale factors [85]. Uncertainties in these scale factors arise from a variety of effects, including variations in the jet energy scales, the finite size of the samples used to measure the scale factors, and background contamination in the data regions used to measure the scale factors. The uncertainties in the scale factors for each effect are treated as nuisance parameters, some of which are correlated from year to year and some of which are independent for each year. Similarly, the efficiency of the DEEPAK8 $\mathrm{b\bar{b}}$ tagger is corrected in simulation to better match the data, and the uncertainty in this correction is treated independently for each year.

8 Results

Using the discriminating variables described in Section 6, namely the boson candidate AK8 jet p_{T}, its m_{SD}, and the full event neural network score, we measure the signal strengths of boosted $\mathrm{t\bar{t}Z}$ and $\mathrm{t\bar{t}H}$ production, determine 95% confidence level (CL) upper limits on $\mathrm{t\bar{t}Z}$ and $\mathrm{t\bar{t}H}$ cross sections, and constrain the effects of BSM physics arising from dimension-six operators in an EFT framework.

To perform these measurements, we use binned maximum likelihood fits, in which the signal and background model is compared to the data in each bin. The likelihood function used to fit the data is the Poisson likelihood with a rate described by the signal and background model,

$$L_{\mathrm{data}}\left(\boldsymbol{\theta}_{\mathrm{POI}}, \boldsymbol{\theta}_{\mathrm{nuis}} \mid D_{\mathrm{i}}\right) = \prod_{\mathrm{i}} \frac{\lambda_{\mathrm{i}}\left(\boldsymbol{\theta}_{\mathrm{POI}}, \boldsymbol{\theta}_{\mathrm{nuis}}\right)^{D_{\mathrm{i}}} e^{-\lambda_{\mathrm{i}}\left(\boldsymbol{\theta}_{\mathrm{POI}}, \boldsymbol{\theta}_{\mathrm{nuis}}\right)}}{D_{\mathrm{i}}!},$$

where

$$\lambda_{\mathrm{i}}\left(\boldsymbol{\theta}_{\mathrm{POI}}, \boldsymbol{\theta}_{\mathrm{nuis}}\right) = S_{\mathrm{i}}\left(\boldsymbol{\theta}_{\mathrm{POI}}, \boldsymbol{\theta}_{\mathrm{nuis}}\right) + B_{\mathrm{i}}\left(\boldsymbol{\theta}_{\mathrm{nuis}}\right)$$

and where i is a bin index, which runs over all the bins, D_{i} is the number of observed events, S_{i} is the number of events predicted by the signal model, B_{i} is the number of predicted background events, $\boldsymbol{\theta}_{\mathrm{POI}}$ is the set of parameters of interest (POIs), and $\boldsymbol{\theta}_{\mathrm{nuis}}$ is the set of nuisance parameters. The background model depends only on the nuisance parameters, while the signal model depends on both the nuisance parameters and the POIs. The overall likelihood function is the product of L_{data} and the constraint factors for each of the nuisance parameters, which introduce a likelihood penalty when the nuisance parameters shift from their nominal values. The constraint factors are Gaussian with a few exceptions, which are detailed in Section 7. The $\mathrm{t\bar{t}} + \mathrm{b\bar{b}}$ rate is only constrained to be positive and otherwise is unconstrained in the fit. The

Table 3: The observed and expected best fit (± 1 standard deviation) signal strength modifiers $\mu_{t\bar{t}Z}$ and $\mu_{t\bar{t}H}$ for simulated p_T^Z or $p_T^H > 200\,\text{GeV}$. The observed uncertainties are broken down into the components arising from the limited size of the data, the limited size of the simulation samples, experimental uncertainties, and theoretical uncertainties.

Signal strength	Observed	Stat.	MC stat.	Exp. syst.	Theo. syst.	Expected
$\mu_{t\bar{t}Z}$	$0.65^{+1.04}_{-0.98}$	$^{+0.80}_{-0.75}$	$^{+0.36}_{-0.38}$	$^{+0.38}_{-0.31}$	$^{+0.43}_{-0.38}$	$1.00^{+0.91}_{-0.84}$
$\mu_{t\bar{t}H}$	$-0.27^{+0.86}_{-0.83}$	$^{+0.72}_{-0.65}$	$^{+0.31}_{-0.33}$	$^{+0.19}_{-0.19}$	$^{+0.28}_{-0.35}$	$1.00^{+0.79}_{-0.72}$

factors representing the statistical uncertainties in the simulation use the approach described in Ref. [92].

For each fit, the likelihood function is maximized in terms of both the POIs and the nuisance parameters in order to obtain the best fit values of the POIs. Confidence intervals for the POIs are obtained by profiling the likelihood ratio [98], where the denominator is the maximized likelihood and the numerator is the maximized likelihood given a fixed value for one or more POIs. We perform one-dimensional and two-dimensional scans of the likelihood ratio in which one or two POIs are repeatedly fixed to specific values while the likelihood is maximized as a function of all the remaining parameters. The 95% CL upper limits are set with the asymptotic approximation [99] of the modified frequentist CL_s criterion [100, 101], in which the profile likelihood ratio is modified for upper limits [98] and used as the test statistic.

We validate the results by comparing them to the results we would obtain by considering each data-taking year independently. The results from each year are in agreement with each other and with the full results.

The observed yields in the 198 analysis bins are shown in Fig. 6, together with the expected yields from signal and background processes as predicted by the SM simulation, after fitting to the data (postfit).

8.1 Signal strengths and upper limits on differential cross sections

To facilitate comparisons with theoretical predictions, we isolate and remove the effects of limited detector acceptance and response to $t\bar{t}Z$ and $t\bar{t}H$ production using a maximum likelihood unfolding technique as described in Section 5 of Ref. [102]. Using this technique, we perform a measurement of the signal strengths of boosted $t\bar{t}Z$ and $t\bar{t}H$ production, i.e., the ratios of the measured $t\bar{t}Z$ and $t\bar{t}H$ production cross sections to the cross sections predicted by the SM as defined in Section 3. The measurement is performed in the region of generator-level phase space defined by the rapidity requirement $|y_{Z/H}| < 2.5$ and $p_T^{Z/H} > 200\,\text{GeV}$. The POIs that affect the signal model are the $t\bar{t}Z$ and $t\bar{t}H$ production signal strengths, $\mu_{t\bar{t}Z}$ and $\mu_{t\bar{t}H}$, respectively. The results are shown in Fig. 7 and Table 3, and the impacts $\Delta\mu$ on $\mu_{t\bar{t}Z}$ versus $\mu_{t\bar{t}H}$ from the major sources of systematic uncertainty are listed in Table 4. The $\Delta\mu$ for $t\bar{t}Z$ and $t\bar{t}H$ are obtained by freezing one group of nuisance parameters at a time, and subtracting, in quadrature, the resulting 68% interval from the full fit interval. The observed correlation between $\mu_{t\bar{t}Z}$ and $\mu_{t\bar{t}H}$ is -10%. The observed yield for the $t\bar{t} + b\bar{b}$ background is higher than the nominal SM prediction from the MC simulation, but it is consistent with the findings of other CMS measurements [96, 103, 104].

Because the uncertainties in the boosted $t\bar{t}Z$ and $t\bar{t}H$ cross sections are large, we are not able to provide two-sided confidence intervals in individual bins of p_T^Z and p_T^H. Instead, we pro-

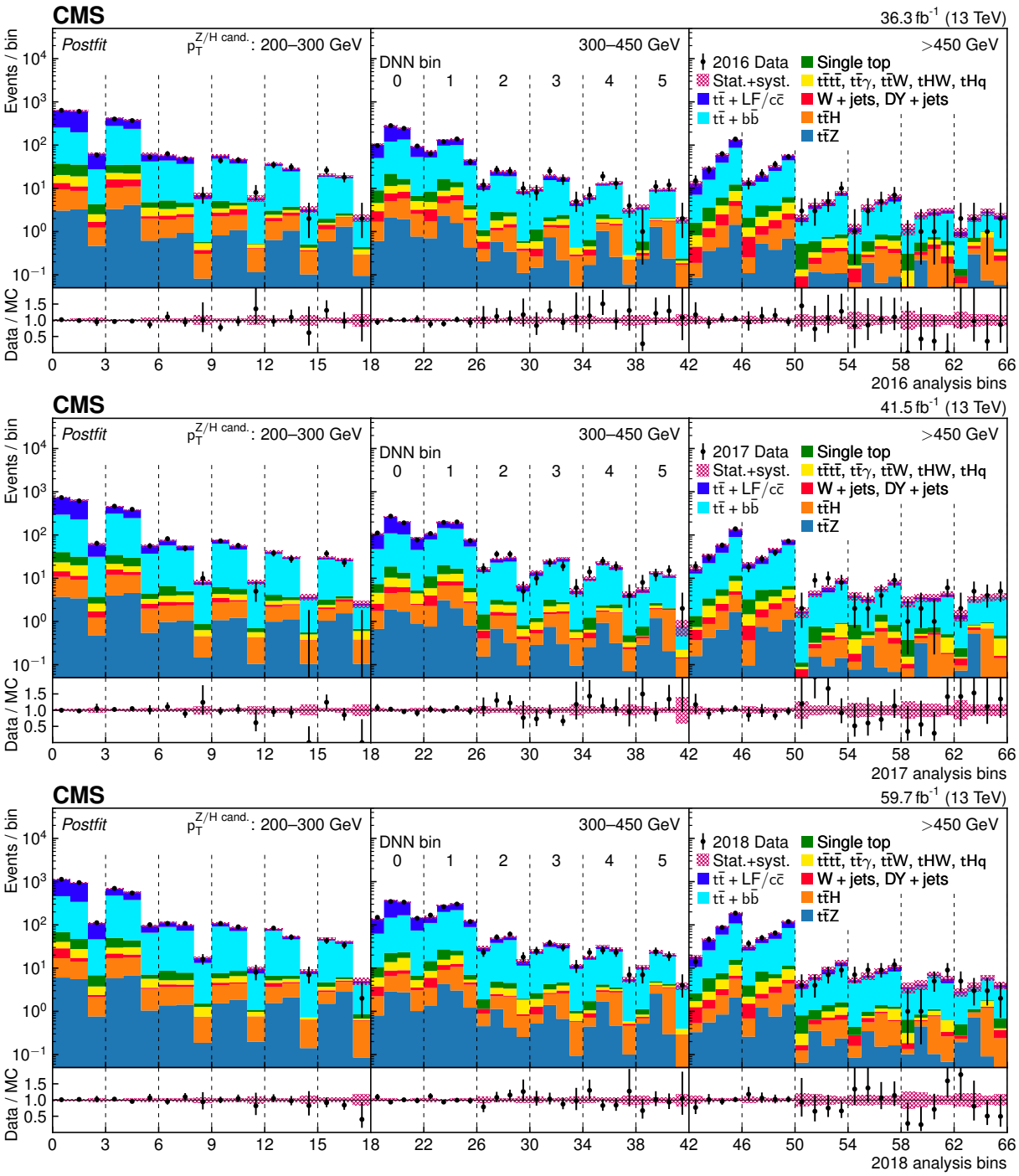

Figure 6: Postfit expected (solid histograms) and observed (points) yields for the 2016 (upper), 2017 (middle), and 2018 (lower) data-taking periods in each analysis bin. In the fit, the $\mathrm{t\bar{t}Z}$ and $\mathrm{t\bar{t}H}$ signal cross sections are fixed to the SM predictions. The analysis bins are defined as functions of the DNN score, and the p_{T} and m_{SD} of the boson candidate AK8 jet. The largest three groupings of bins in each year are defined by the AK8 jet p_{T}. The next six groups are defined by the DNN score, and the smallest groups of three or four bins with the same p_{T} and DNN score correspond to the AK8 jet m_{SD}. The vertical bars on the points show the statistical uncertainty in the data. The lower panels in each plot give the ratio of the data to the sum of the MC predictions, with the red band representing the total uncertainty in the MC prediction.

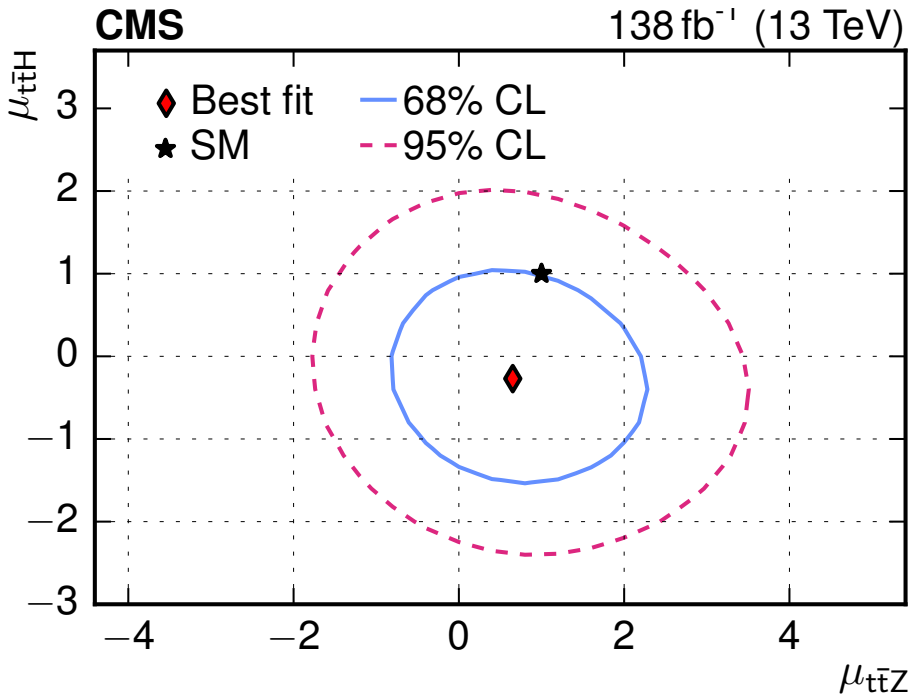

Figure 7: The observed best fit values (diamond) and SM predictions (star) for the signal strength modifiers $\mu_{t\bar{t}H}$ versus $\mu_{t\bar{t}Z}$ for generator-level p_T^H or $p_T^Z > 200\,\text{GeV}$. The solid blue and dashed red contours show the 68 and 95% CL regions, respectively.

Table 4: The magnitudes of the major sources of systematic uncertainty in the measurement of the signal strength modifiers $\mu_{t\bar{t}Z}$ and $\mu_{t\bar{t}H}$ for simulated p_T^Z or $p_T^H > 200\,\text{GeV}$.

Source of uncertainty	$\Delta\mu_{t\bar{t}Z}$	$\Delta\mu_{t\bar{t}H}$
$t\bar{t} + c\bar{c}$ cross section	$^{+0.27}_{-0.23}$	$^{+0.14}_{-0.13}$
$t\bar{t} + b\bar{b}$ cross section	$^{+0.18}_{-0.24}$	$^{+0.16}_{-0.22}$
$t\bar{t} + 2b$ cross section	$^{+0.03}_{-0.03}$	±0.09
μ_R and μ_F scales	$^{+0.12}_{-0.14}$	$^{+0.11}_{-0.15}$
Parton shower	$^{+0.16}_{-0.17}$	$^{+0.07}_{-0.06}$
b tagging efficiency	$^{+0.25}_{-0.13}$	±0.10
$b\bar{b}$ tagging efficiency	$^{+0.18}_{-0.13}$	$^{+0.07}_{-0.04}$
Jet energy scale and resolution	±0.11	$^{+0.11}_{-0.12}$
Jet mass scale and resolution	±0.10	±0.08

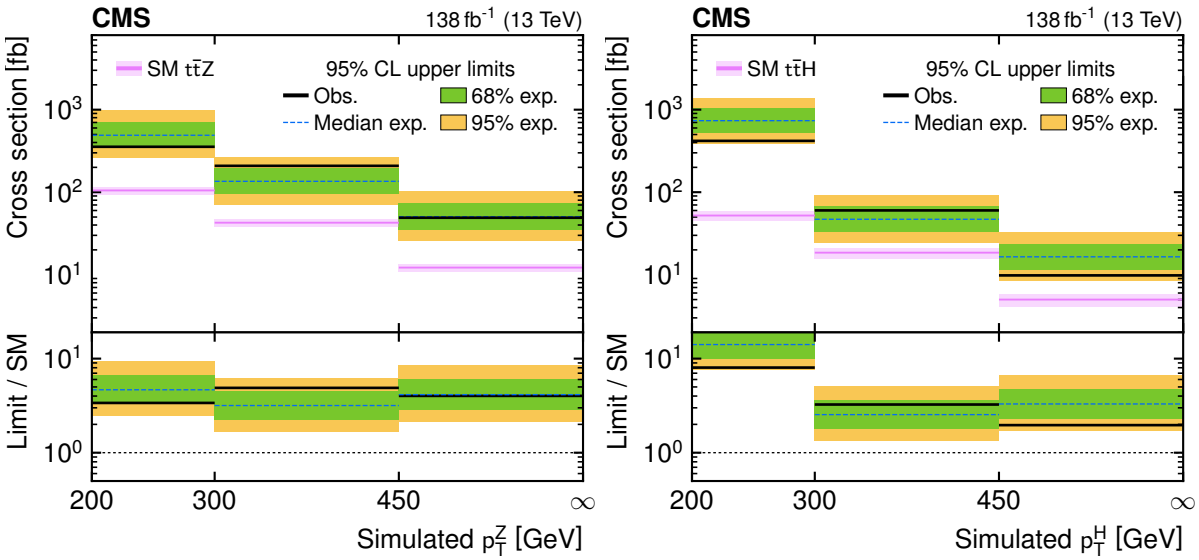

Figure 8: Observed and expected 95% CL upper limits on the $t\bar{t}Z$ (left) and $t\bar{t}H$ (right) differential cross sections as a function of the simulated Z and Higgs boson p_T. The green and yellow bands indicate the regions containing 68 and 95%, respectively, of the distribution of limits under the SM hypothesis. The black lines represent the observed 95% CL upper limits. The magenta band shows the SM predicted differential cross sections with the PDF + α_S and scale uncertainties. The lower panel shows the ratio of the observed and expected upper limits on the differential cross sections to the SM differential cross sections. The last bin is unbounded.

vide 95% CL upper limits on the differential cross sections for production of $t\bar{t}Z$ and $t\bar{t}H$ as functions of p_T^Z and p_T^H. We account for smearing of the reconstructed p_T^Z and p_T^H compared to the simulated quantities using folding matrices, which are similar to those shown in Fig. 5, but expanded to include the DNN score and m_{SD}. Like the signal strength measurement, these upper limits are established in the region of generator-level phase space defined by $|y_{Z/H}| < 2.5$ and $p_T^{Z/H} > 200\,\text{GeV}$. Simulated $t\bar{t}Z$ and $t\bar{t}H$ events are divided into subsamples according to the simulated p_T^Z and p_T^H, which, along with the cross section corresponding to each subsample, form the signal model and its POIs. When setting the upper limit on one differential cross section, the other differential cross sections are profiled. The 95% CL upper limits on the differential cross sections are given in Fig. 8 and Table 5.

8.2 Effective field theory constraints

We constrain eight WCs from the LO dimension-six EFT model described in Section 3.1. Again, we impose a generator-level requirement on the rapidity of the Z or Higgs boson, $|y_{Z/H}| < 2.5$. The effects of varying the WCs are computed as a weight w_{EFT} for each simulated event in the $t\bar{t}Z$, $t\bar{t}H$, and $t\bar{t} + b\bar{b}$ samples, detailed in Eq. (1). This weight affects the predicted yields in each analysis bin, as described in Section 8.1. For each bin, we compute the ratio of the expected rate in the EFT model to the expected rate in the LO SM, as a function of the WCs. The LO SM expected yields are multiplied by this ratio in each bin and by an NLO K factor, which is the ratio of the expected NLO SM yield to the expected LO SM yield. This produces predicted NLO histograms parameterized in the WCs. Thus, the signal yield in each bin is expressed as

$$\text{bin yield} = \text{LO SM yield} \times \frac{\text{NLO SM yield}}{\text{LO SM yield}} \times \frac{\text{LO EFT yield}}{\text{LO SM yield}}.$$

Table 5: Observed and median expected 95% CL upper limits on the $t\bar{t}Z$ and $t\bar{t}H$ differential cross sections and on their ratios to the SM predictions for three $p_T^{Z/H}$ intervals. The range given with the median expected 95% CL upper limits indicates the range in which 68% of the upper limits are expected to fall, assuming the SM hypothesis.

Signal	$p_T^{Z/H}$ interval [GeV]	95% CL upper limit [fb]		95% CL upper limit / SM	
		Observed	Expected	Observed	Expected
$t\bar{t}Z$	200–300	360	490^{+210}_{-140}	3.4	$4.7^{+2.0}_{-1.4}$
	300–450	209	135^{+58}_{-40}	4.9	$3.2^{+1.4}_{-0.9}$
	>450	49	51^{+23}_{-15}	4.0	$4.1^{+1.9}_{-1.3}$
$t\bar{t}H$	200–300	420	740^{+300}_{-210}	8.0	$14.1^{+5.7}_{-4.1}$
	300–450	60	47^{+20}_{-14}	3.2	$2.5^{+1.1}_{-0.8}$
	>450	9.8	$16.5^{+7.3}_{-4.9}$	2.0	$3.3^{+1.5}_{-1.0}$

We maximize the likelihood function in terms of the WCs and the various nuisance parameters representing the systematic uncertainties.

We perform a likelihood scan for each WC while fixing the seven other WCs to their SM value of zero. With the WCs fixed, we find the maximum likelihood as a function of the nuisance parameters. We extract 68 and 95% CL intervals from the resulting profiled likelihood as shown in Fig. 9. We also perform a second scan for each WC in which the seven other WCs are not fixed, so that the likelihood is maximized as a function of the nuisance parameters and seven of the eight WCs. Both sets of intervals are summarized in Fig. 10, and the 95% CL intervals are summarized in Table 6. Because of partial degeneracies in the effects of the WCs, the constraints on the WCs from the two different likelihood scans tend to differ for $c^-_{\varphi Q}$, $c^3_{\varphi Q}$, $c_{\varphi t}$, c_{tW}, and c_{tZ}. To further explore this, two-dimensional likelihood scans are performed for pairs of WCs while the remaining six WCs are fixed to zero. Figure 11 shows the 68, 95, and 99.7% CL regions extracted from the scans for the three pairs of WCs that exhibit the largest postfit correlations. As shown in Table 1, two of these WC pairs ($c^3_{\varphi Q}$, $c^-_{\varphi Q}$) and (c_{tW}, c_{tZ}) apply to the same operators $O^{(ij)}_{\varphi q}$ and $O^{(ij)}_{uB}$, respectively, and the other WC pair ($c_{\varphi t}$, $c^-_{\varphi Q}$) corresponds to the operators $O^{(ij)}_{\varphi u}$ and $O^{(ij)}_{\varphi q}$, which have a similar structure, leading to the observed correlations.

The likelihood scans for the WCs are sometimes bimodal, as can be seen in Fig. 9 for $c_{t\varphi}$ and c_{bW}. This arises because the predicted yields in each analysis bin are quadratic as functions of the WCs, so the observed or expected yields may be most consistent with the predictions at two distinct WC values. The observed WC constraints are tighter than expected because the observed yields of $t\bar{t} + b\bar{b}$ and $t\bar{t}H$ are higher and lower, respectively, than the SM expectations. All of the WC constraints are in close agreement with the SM with the exception of $c_{t\varphi}$, which shows a weak tension with the SM. This tension is dominated by the yield of $t\bar{t}H$, which is smaller than expected, as seen in Figs. 7 and 8.

Figure 12 compares the 95% CL intervals from this analysis with previous CMS measurements, which used events with multiple leptons or photons [16, 25, 27, 28]. There is good agreement among the various results, and in some cases the limits from this analysis are comparable to the best previously published limits.

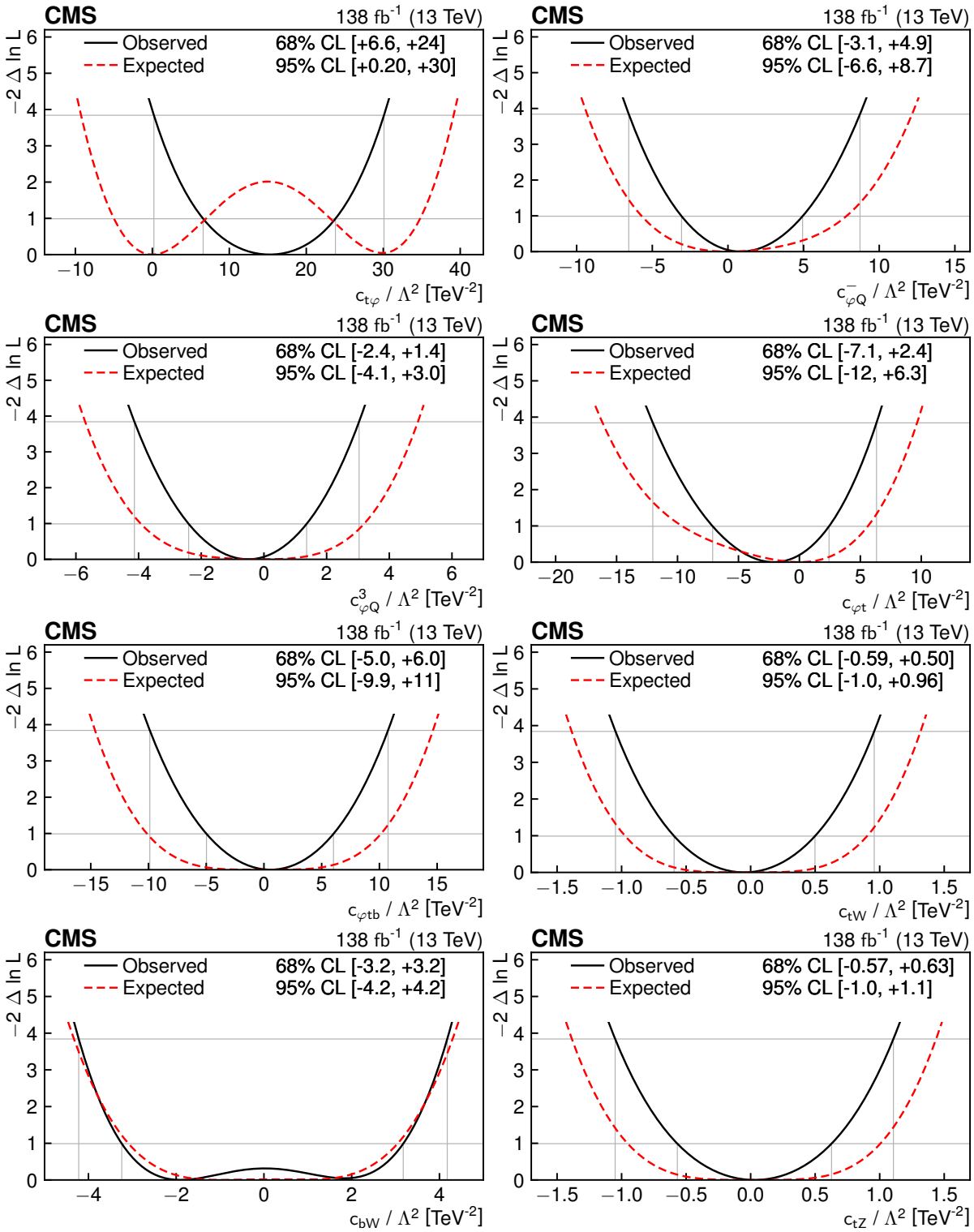

Figure 9: Observed (solid black) and expected (dotted red) scans of the negative log-likelihood as a function of each of the eight WCs when the seven other WCs are fixed to their SM values. The 68 and 95% CL intervals are indicated by thin gray lines.

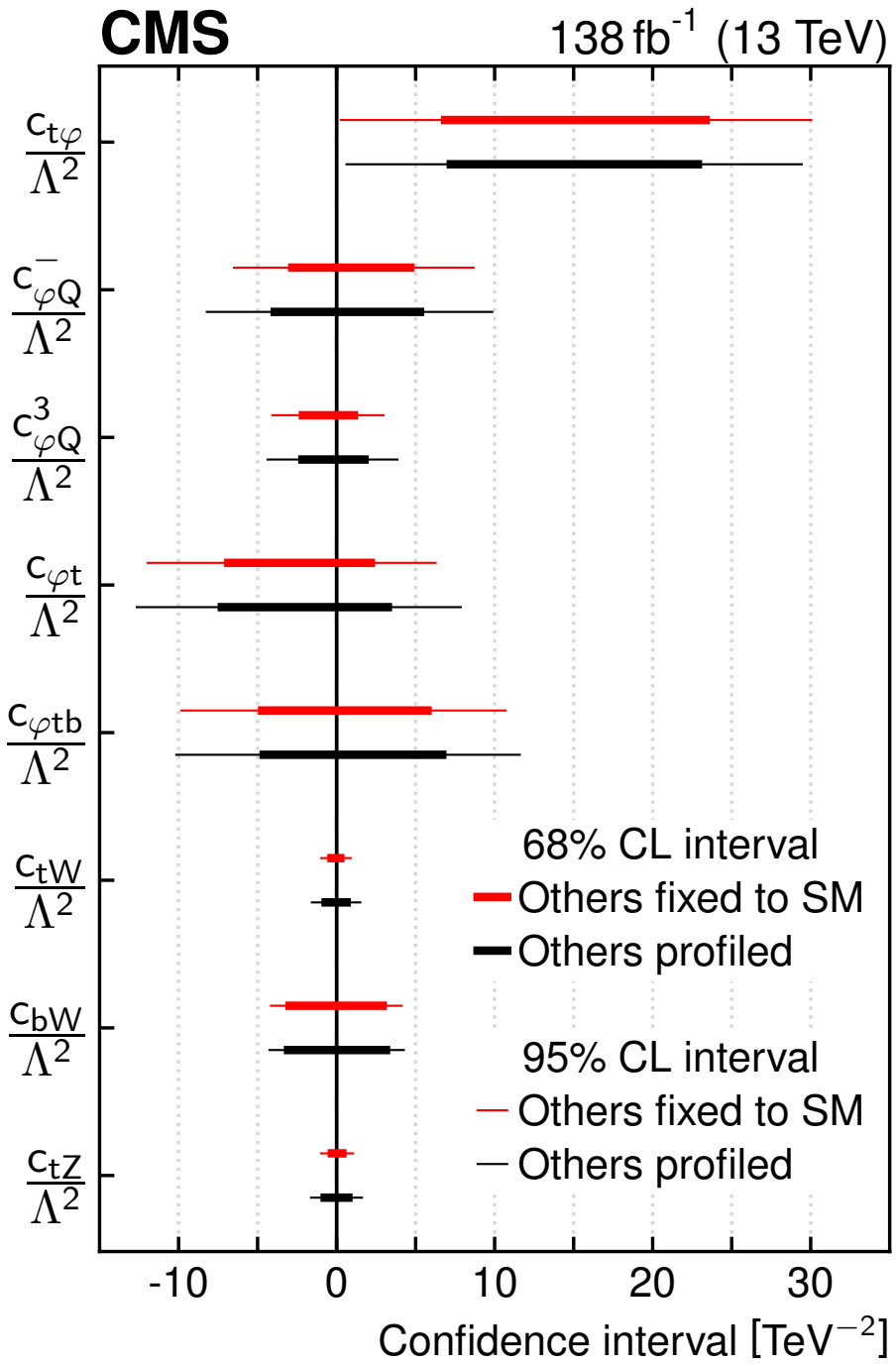

Figure 10: The observed 68 and 95% CL intervals for the WCs are shown by the thick and thin bars, respectively. The intervals are found by scanning over a single WC while either profiling the other seven WCs (black) or fixing them to the SM value of zero (red).

Table 6: Observed 95% CL intervals for the eight WCs in the EFT model. The intervals are determined by scanning over a single WC while either profiling the other seven WCs or fixing them to their SM value of zero.

WC/Λ^2	95% CL interval [TeV^{-2}]	
	(Others profiled)	(Others fixed to SM)
$c_{\mathrm{t}\varphi}/\Lambda^2$	[0.56, 30]	[0.20, 30]
$c^{-}_{\varphi\mathrm{Q}}/\Lambda^2$	[−8.3, 9.9]	[−6.6, 8.7]
$c^{3}_{\varphi\mathrm{Q}}/\Lambda^2$	[−4.4, 3.9]	[−4.1, 3.0]
$c_{\varphi\mathrm{t}}/\Lambda^2$	[−13, 7.9]	[−12, 6.3]
$c_{\varphi\mathrm{tb}}/\Lambda^2$	[−10, 12]	[−9.9, 11]
$c_{\mathrm{tW}}/\Lambda^2$	[−1.6, 1.6]	[−1.0, 0.96]
$c_{\mathrm{bW}}/\Lambda^2$	[−4.3, 4.3]	[−4.2, 4.2]
$c_{\mathrm{tZ}}/\Lambda^2$	[−1.7, 1.7]	[−1.0, 1.1]

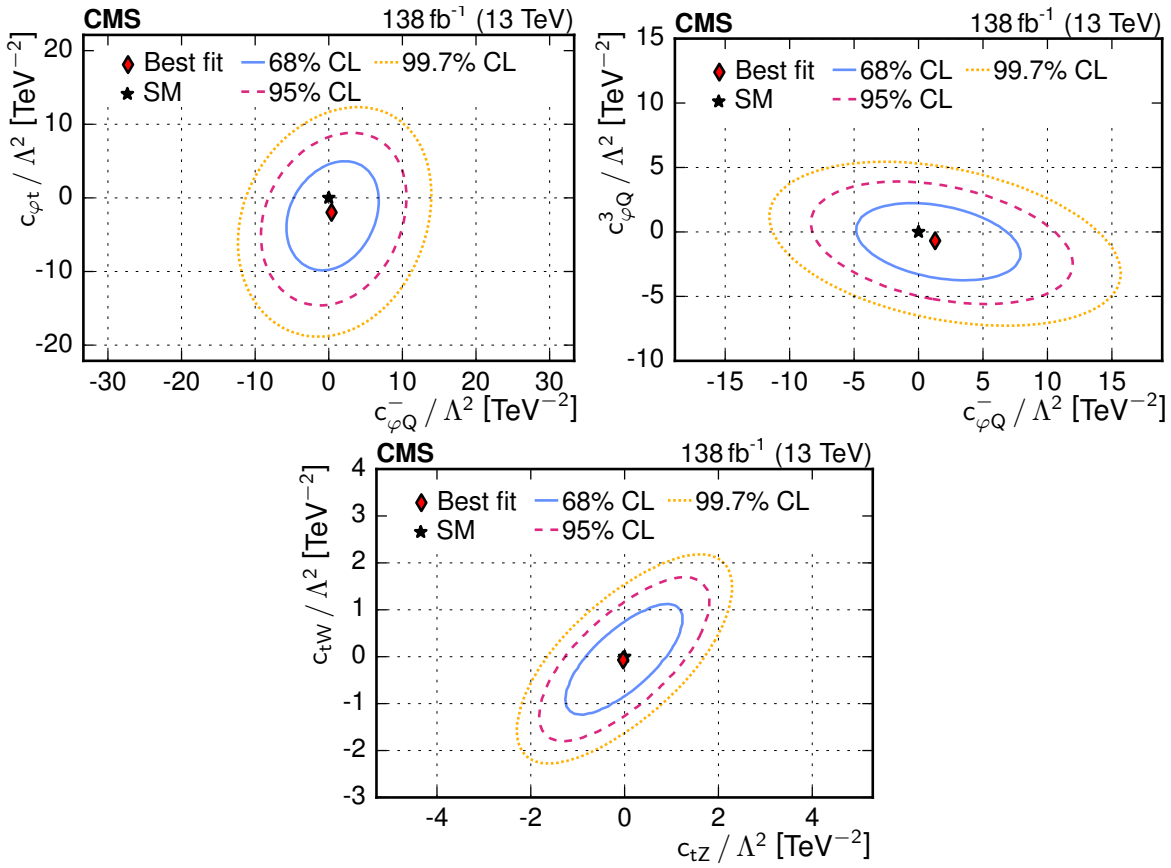

Figure 11: Observed two-dimensional scans of the negative log-likelihood as a function of two of the eight WCs when all other WCs are fixed to their SM values. The three pairs of WCs scanned have the three largest observed correlation coefficients among all pairs. They are $c_{\varphi\mathrm{t}}$ versus $c^{-}_{\varphi\mathrm{Q}}$ (upper left), $c^{3}_{\varphi\mathrm{Q}}$ versus $c^{-}_{\varphi\mathrm{Q}}$ (upper right), and c_{tW} versus c_{tZ} (lower). The 68, 95, and 99.7% CL intervals are indicated by the solid blue, dashed red, and dotted orange lines, respectively.

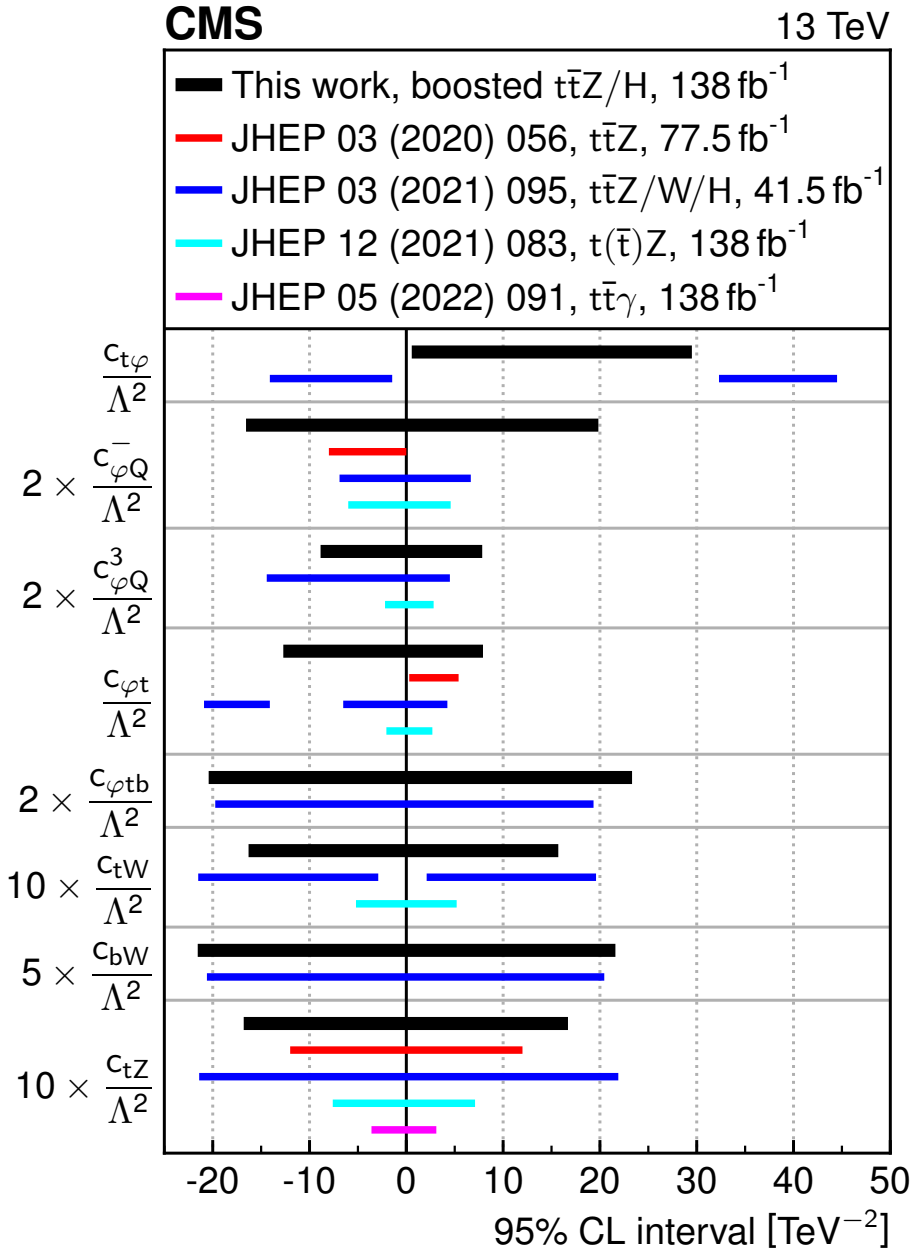

Figure 12: Observed 95% CL intervals for the WCs. The intervals are found by scanning over a single WC while fixing the other seven to zero. For comparison, we also show the corresponding 95% CL intervals from Refs. [16, 25, 27, 28], which used events with multiple leptons or photons. The intervals for several of the WCs would be too small to see clearly, and so we have increased their size by the factor given in the label on the left edge of the figure.

9 Summary

Measurements of the signal strengths and 95% confidence level upper limits on the differential cross sections for production of $\mathrm{t\bar{t}Z}$ and $\mathrm{t\bar{t}H}$ events, where H refers to the Higgs boson, are presented along with constraints on the Wilson coefficients of a leading-order effective field theory. The analysis is performed using the $\mathrm{b\bar{b}}$ decay mode of the Z or Higgs boson and the lepton plus jets channel of the associated $\mathrm{t\bar{t}}$ pair. The Z or Higgs boson is required to be Lorentz boosted, with transverse momentum $p_{\mathrm{T}} > 200\,\mathrm{GeV}$. A deep neural network is employed to discriminate between the $\mathrm{t\bar{t}Z}$ and $\mathrm{t\bar{t}H}$ signal events and the background, which is dominated by $\mathrm{t\bar{t}}+\mathrm{jets}$ production. The data correspond to an integrated luminosity of $138\,\mathrm{fb}^{-1}$ collected with the CMS detector at the CERN LHC from 2016 through 2018. The data are binned as a function of the deep neural network score and the reconstructed p_{T} and mass of the Z or Higgs boson. Binned maximum likelihood fits are employed to extract the observables from the data.

The data are found to be consistent with the expectations from the standard model. The signal strength modifiers for boosted $\mathrm{t\bar{t}Z}$ and $\mathrm{t\bar{t}H}$ production are measured to be $\mu_{\mathrm{t\bar{t}Z}} = 0.65^{+1.04}_{-0.98}$ and $\mu_{\mathrm{t\bar{t}H}} = -0.27^{+0.86}_{-0.83}$, which are both consistent with the expected value, 1. The 95% confidence level upper limits on the differential $\mathrm{t\bar{t}Z}$ and $\mathrm{t\bar{t}H}$ cross sections range from 2 to 5 times the standard model predicted cross sections for Z or Higgs boson $p_{\mathrm{T}} > 300\,\mathrm{GeV}$. Results are also presented on eight parameters of a leading-order effective field theory that have a large impact on boosted $\mathrm{t\bar{t}Z}$ and $\mathrm{t\bar{t}H}$ production. These results represent the most restrictive limits to date on the cross sections for the production of $\mathrm{t\bar{t}Z}$ and $\mathrm{t\bar{t}H}$ with Z or Higgs boson $p_{\mathrm{T}} > 450\,\mathrm{GeV}$. The limits on the Wilson coefficients in the effective field theory are consistent and, in some cases, competitive with the best previous limits.

References

[1] V. C. Rubin and W. K. Ford, Jr., "Rotation of the Andromeda nebula from a spectroscopic survey of emission regions", *Astrophys. J.* **159** (1970) 379, doi:10.1086/150317.

[2] Planck Collaboration, "Planck 2018 results. VI. cosmological parameters", *Astron. Astrophys.* **641** (2020) A6, doi:10.1051/0004-6361/201833910, arXiv:1807.06209. [Erratum: doi:10.1051/0004-6361/201833910e].

[3] D. Clowe, A. Gonzalez, and M. Markevitch, "Weak lensing mass reconstruction of the interacting cluster 1E 0657-558: Direct evidence for the existence of dark matter", *Astrophys. J.* **604** (2004) 596, doi:10.1086/381970, arXiv:astro-ph/0312273.

[4] R. K. Kaul and P. Majumdar, "Cancellation of quadratically divergent mass corrections in globally supersymmetric spontaneously broken gauge theories", *Nucl. Phys. B* **199** (1982) 36, doi:10.1016/0550-3213(82)90565-X.

[5] R. Barbieri and G. F. Giudice, "Upper bounds on supersymmetric particle masses", *Nucl. Phys. B* **306** (1988) 63, doi:10.1016/0550-3213(88)90171-X.

[6] W. Buchmüller and D. Wyler, "Effective Lagrangian analysis of new interactions and flavor conservation", *Nucl. Phys. B* **268** (1986) 621, doi:10.1016/0550-3213(86)90262-2.

[7] B. Grzadkowski, M. Iskrzyński, M. Misiak, and J. Rosiek, "Dimension-six terms in the standard model Lagrangian", *JHEP* **10** (2010) 085, doi:10.1007/JHEP10(2010)085, arXiv:1008.4884.

[8] A. Falkowski and R. Rattazzi, "Which EFT", *JHEP* **10** (2019) 255, doi:10.1007/JHEP10(2019)255, arXiv:1902.05936.

[9] C. Degrande et al., "Effective field theory: A modern approach to anomalous couplings", *Annals Phys.* **335** (2013) 21, doi:10.1016/j.aop.2013.04.016, arXiv:1205.4231.

[10] A. Kobach, "Baryon number, lepton number, and operator dimension in the standard model", *Phys. Lett. B* **758** (2016) 455, doi:10.1016/j.physletb.2016.05.050, arXiv:1604.05726.

[11] Particle Data Group, P. A. Zyla et al., "Review of particle physics", *Prog. Theor. Exp. Phys.* **2020** (2020) 083C01, doi:10.1093/ptep/ptaa104.

[12] J. A. Aguilar-Saavedra et al., "Interpreting top-quark LHC measurements in the standard-model effective field theory", LHC TOP WG note CERN-LPCC-2018-01, 2018. arXiv:1802.07237.

[13] ATLAS Collaboration, "Measurement of the $t\bar{t}Z$ and $t\bar{t}W$ cross sections in proton-proton collisions at $\sqrt{s} = 13$ TeV with the ATLAS detector", *Phys. Rev. D* **99** (2019) 072009, doi:10.1103/PhysRevD.99.072009, arXiv:1901.03584.

[14] ATLAS Collaboration, "Measurements of the inclusive and differential production cross sections of a top-quark-antiquark pair in association with a Z boson at $\sqrt{s} = 13$ TeV with the ATLAS detector", *Eur. Phys. J. C* **81** (2021) 737, doi:10.1140/epjc/s10052-021-09439-4, arXiv:2103.12603.

[15] CMS Collaboration, "Measurement of the cross section for top quark pair production in association with a W or Z boson in proton-proton collisions at $\sqrt{s} = 13$ TeV", *JHEP* **08** (2018) 011, doi:10.1007/JHEP08(2018)011, arXiv:1711.02547.

[16] CMS Collaboration, "Measurement of top quark pair production in association with a Z boson in proton-proton collisions at $\sqrt{s} = 13$ TeV", *JHEP* **03** (2020) 056, doi:10.1007/JHEP03(2020)056, arXiv:1907.11270.

[17] ATLAS Collaboration, "Observation of Higgs boson production in association with a top quark pair at the LHC with the ATLAS detector", *Phys. Lett. B* **784** (2018) 173, doi:10.1016/j.physletb.2018.07.035, arXiv:1806.00425.

[18] ATLAS Collaboration, "*CP* properties of Higgs boson interactions with top quarks in the $t\bar{t}H$ and tH processes using $H \to \gamma\gamma$ with the ATLAS detector", *Phys. Rev. Lett.* **125** (2020) 061802, doi:10.1103/PhysRevLett.125.061802, arXiv:2004.04545.

[19] ATLAS Collaboration, "Measurement of Higgs boson decay into b-quarks in associated production with a top-quark pair in pp collisions at $\sqrt{s} = 13$ TeV with the ATLAS detector", *JHEP* **06** (2022) 097, doi:10.1007/JHEP06(2022)097, arXiv:2111.06712.

[20] CMS Collaboration, "Observation of $t\bar{t}H$ production", *Phys. Rev. Lett.* **120** (2018) 231801, doi:10.1103/PhysRevLett.120.231801, arXiv:1804.02610.

[21] CMS Collaboration, "Search for $t\bar{t}H$ production in the all-jet final state in proton-proton collisions at $\sqrt{s} = 13$ TeV", *JHEP* **06** (2018) 101, doi:10.1007/JHEP06(2018)101, arXiv:1803.06986.

[22] CMS Collaboration, "Search for $\mathrm{t\bar{t}H}$ production in the $\mathrm{H} \to \mathrm{b\bar{b}}$ decay channel with leptonic $\mathrm{t\bar{t}}$ decays in proton-proton collisions at $\sqrt{s} = 13$ TeV", *JHEP* **03** (2019) 026, doi:10.1007/JHEP03(2019)026, arXiv:1804.03682.

[23] CMS Collaboration, "Measurements of $\mathrm{t\bar{t}H}$ production and the *CP* structure of the Yukawa interaction between the Higgs boson and top quark in the diphoton decay channel", *Phys. Rev. Lett.* **125** (2020) 061801, doi:10.1103/PhysRevLett.125.061801, arXiv:2003.10866.

[24] CMS Collaboration, "Measurement of the Higgs boson production rate in association with top quarks in final states with electrons, muons, and hadronically decaying tau leptons at $\sqrt{s} = 13$ TeV", *Eur. Phys. J. C* **81** (2021) 378, doi:10.1140/epjc/s10052-021-09014-x, arXiv:2011.03652.

[25] CMS Collaboration, "Search for new physics in top quark production with additional leptons in proton-proton collisions at $\sqrt{s} = 13$ TeV using effective field theory", *JHEP* **03** (2021) 095, doi:10.1007/JHEP03(2021)095, arXiv:2012.04120.

[26] CMS Collaboration, "Measurement of the inclusive and differential $\mathrm{t\bar{t}}\gamma$ cross sections in the single-lepton channel and EFT interpretation at $\sqrt{s} = 13$ TeV", *JHEP* **12** (2021) 180, doi:10.1007/JHEP12(2021)180, arXiv:2107.01508.

[27] CMS Collaboration, "Probing effective field theory operators in the associated production of top quarks with a Z boson in multilepton final states at $\sqrt{s} = 13$ TeV", *JHEP* **12** (2021) 083, doi:10.1007/JHEP12(2021)083, arXiv:2107.13896.

[28] CMS Collaboration, "Measurement of the inclusive and differential $\mathrm{t\bar{t}}\gamma$ cross sections in the dilepton channel and effective field theory interpretation in proton-proton collisions at $\sqrt{s} = 13$ TeV", *JHEP* **05** (2022) 091, doi:10.1007/JHEP05(2022)091, arXiv:2201.07301.

[29] HEPData record for this analysis, 2022. doi:10.17182/hepdata.127700.

[30] CMS Collaboration, "Performance of the CMS Level-1 trigger in proton-proton collisions at $\sqrt{s} = 13$ TeV", *JINST* **15** (2020) P10017, doi:10.1088/1748-0221/15/10/P10017, arXiv:2006.10165.

[31] CMS Collaboration, "The CMS trigger system", *JINST* **12** (2017) P01020, doi:10.1088/1748-0221/12/01/P01020, arXiv:1609.02366.

[32] CMS Collaboration, "The CMS experiment at the CERN LHC", *JINST* **3** (2008) S08004, doi:10.1088/1748-0221/3/08/S08004.

[33] CMS Collaboration, "Precision luminosity measurement in proton-proton collisions at $\sqrt{s} = 13$ TeV in 2015 and 2016 at CMS", *Eur. Phys. J. C* **81** (2021) 800, doi:10.1140/epjc/s10052-021-09538-2, arXiv:2104.01927.

[34] CMS Collaboration, "CMS luminosity measurement for the 2017 data-taking period at $\sqrt{s} = 13$ TeV", CMS Physics Analysis Summary CMS-PAS-LUM-17-004, 2018.

[35] CMS Collaboration, "CMS luminosity measurement for the 2018 data-taking period at $\sqrt{s} = 13$ TeV", CMS Physics Analysis Summary CMS-PAS-LUM-18-002, 2019.

[36] J. Alwall et al., "The automated computation of tree-level and next-to-leading order differential cross sections, and their matching to parton shower simulations", *JHEP* **07** (2014) 079, doi:10.1007/JHEP07(2014)079, arXiv:1405.0301.

[37] P. Nason, "A new method for combining NLO QCD with shower Monte Carlo algorithms", *JHEP* **11** (2004) 040, doi:10.1088/1126-6708/2004/11/040, arXiv:hep-ph/0409146.

[38] S. Frixione, P. Nason, and C. Oleari, "Matching NLO QCD computations with parton shower simulations: the POWHEG method", *JHEP* **11** (2007) 070, doi:10.1088/1126-6708/2007/11/070, arXiv:0709.2092.

[39] S. Alioli, P. Nason, C. Oleari, and E. Re, "A general framework for implementing NLO calculations in shower Monte Carlo programs: the POWHEG BOX", *JHEP* **06** (2010) 043, doi:10.1007/JHEP06(2010)043, arXiv:1002.2581.

[40] H. B. Hartanto, B. Jäger, L. Reina, and D. Wackeroth, "Higgs boson production in association with top quarks in the POWHEG BOX", *Phys. Rev. D* **91** (2015) 094003, doi:10.1103/PhysRevD.91.094003, arXiv:1501.04498.

[41] A. Kulesza et al., "Associated production of a top quark pair with a heavy electroweak gauge boson at NLO+NNLL accuracy", *Eur. Phys. J. C* **79** (2019) 249, doi:10.1140/epjc/s10052-019-6746-z, arXiv:1812.08622.

[42] LHC Higgs Cross Section Working Group, "Handbook of LHC Higgs cross sections: 4. Deciphering the nature of the Higgs sector", CERN Report CERN-2017-002-M, 2016. doi:10.23731/CYRM-2017-002, arXiv:1610.07922.

[43] T. Ježo, J. M. Lindert, N. Moretti, and S. Pozzorini, "New NLOPS predictions for $t\bar{t}$ + b-jet production at the LHC", *Eur. Phys. J. C* **78** (2018) 502, doi:10.1140/epjc/s10052-018-5956-0, arXiv:1802.00426.

[44] F. Buccioni, S. Kallweit, S. Pozzorini, and M. F. Zoller, "NLO QCD predictions for $t\bar{t}b\bar{b}$ production in association with a light jet at the LHC", *JHEP* **12** (2019) 015, doi:10.1007/JHEP12(2019)015, arXiv:1907.13624.

[45] S. Frixione, P. Nason, and G. Ridolfi, "A positive-weight next-to-leading-order Monte Carlo for heavy flavour hadroproduction", *JHEP* **09** (2007) 126, doi:10.1088/1126-6708/2007/09/126, arXiv:0707.3088.

[46] M. Czakon et al., "Top-pair production at the LHC through NNLO QCD and NLO EW", *JHEP* **10** (2017) 186, doi:10.1007/JHEP10(2017)186, arXiv:1705.04105.

[47] M. Beneke, P. Falgari, S. Klein, and C. Schwinn, "Hadronic top-quark pair production with NNLL threshold resummation", *Nucl. Phys. B* **855** (2012) 695, doi:10.1016/j.nuclphysb.2011.10.021, arXiv:1109.1536.

[48] M. Cacciari et al., "Top-pair production at hadron colliders with next-to-next-to-leading logarithmic soft-gluon resummation", *Phys. Lett. B* **710** (2012) 612, doi:10.1016/j.physletb.2012.03.013, arXiv:1111.5869.

[49] P. Bärnreuther, M. Czakon, and A. Mitov, "Percent-level-precision physics at the Tevatron: next-to-next-to-leading order QCD corrections to $q\bar{q} \to t\bar{t} + X$", *Phys. Rev. Lett.* **109** (2012) 132001, doi:10.1103/PhysRevLett.109.132001, arXiv:1204.5201.

[50] M. Czakon and A. Mitov, "NNLO corrections to top-pair production at hadron colliders: the all-fermionic scattering channels", *JHEP* **12** (2012) 054, doi:10.1007/JHEP12(2012)054, arXiv:1207.0236.

[51] M. Czakon and A. Mitov, "NNLO corrections to top pair production at hadron colliders: the quark-gluon reaction", *JHEP* **01** (2013) 080, doi:10.1007/JHEP01(2013)080, arXiv:1210.6832.

[52] M. Czakon, P. Fiedler, and A. Mitov, "Total top-quark pair-production cross section at hadron colliders through $O(\alpha_S^4)$", *Phys. Rev. Lett.* **110** (2013) 252004, doi:10.1103/PhysRevLett.110.252004, arXiv:1303.6254.

[53] M. Czakon and A. Mitov, "Top++: a program for the calculation of the top-pair cross-section at hadron colliders", *Comput. Phys. Commun.* **185** (2014) 2930, doi:10.1016/j.cpc.2014.06.021, arXiv:1112.5675.

[54] S. Alioli, P. Nason, C. Oleari, and E. Re, "NLO single-top production matched with shower in POWHEG: s- and t-channel contributions", *JHEP* **09** (2009) 111, doi:10.1088/1126-6708/2009/09/111, arXiv:0907.4076. [Erratum: doi:10.1007/JHEP02(2010)011].

[55] E. Re, "Single-top Wt-channel production matched with parton showers using the POWHEG method", *Eur. Phys. J. C* **71** (2011) 1547, doi:10.1140/epjc/s10052-011-1547-z, arXiv:1009.2450.

[56] S. Quackenbush, R. Gavin, Y. Li, and F. Petriello, "W physics at the LHC with FEWZ 2.1", *Comput. Phys. Commun.* **184** (2013) 209, doi:10.1016/j.cpc.2012.09.005, arXiv:1201.5896.

[57] Y. Li and F. Petriello, "Combining QCD and electroweak corrections to dilepton production in the framework of the FEWZ simulation code", *Phys. Rev. D* **86** (2012) 094034, doi:10.1103/PhysRevD.86.094034, arXiv:1208.5967.

[58] N. Kidonakis, "Two-loop soft anomalous dimensions for single top quark associated production with a W^- or H^-", *Phys. Rev. D* **82** (2010) 054018, doi:10.1103/PhysRevD.82.054018, arXiv:1005.4451.

[59] M. Aliev et al., "HATHOR: hadronic top and heavy quarks cross section calculator", *Comput. Phys. Commun.* **182** (2011) 1034, doi:10.1016/j.cpc.2010.12.040, arXiv:1007.1327.

[60] P. Kant et al., "HATHOR for single top-quark production: updated predictions and uncertainty estimates for single top-quark production in hadronic collisions", *Comput. Phys. Commun.* **191** (2015) 74, doi:10.1016/j.cpc.2015.02.001, arXiv:1406.4403.

[61] R. Frederix and S. Frixione, "Merging meets matching in MC@NLO", *JHEP* **12** (2012) 061, doi:10.1007/JHEP12(2012)061, arXiv:1209.6215.

[62] M. L. Mangano, M. Moretti, F. Piccinini, and M. Treccani, "Matching matrix elements and shower evolution for top-pair production in hadronic collisions", *JHEP* **01** (2007) 013, doi:10.1088/1126-6708/2007/01/013, arXiv:hep-ph/0611129.

[63] CMS Collaboration, "Extraction and validation of a new set of CMS PYTHIA8 tunes from underlying-event measurements", *Eur. Phys. J. C* **80** (2020) 4, doi:10.1140/epjc/s10052-019-7499-4, arXiv:1903.12179.

[64] CMS Collaboration, "Event generator tunes obtained from underlying event and multiparton scattering measurements", *Eur. Phys. J. C* **76** (2016) 155, doi:10.1140/epjc/s10052-016-3988-x, arXiv:1512.00815.

[65] NNPDF Collaboration, "Parton distributions from high-precision collider data", *Eur. Phys. J. C* **77** (2017) 663, doi:10.1140/epjc/s10052-017-5199-5, arXiv:1706.00428.

[66] NNPDF Collaboration, "Parton distributions for the LHC run II", *JHEP* **04** (2015) 040, doi:10.1007/JHEP04(2015)040, arXiv:1410.8849.

[67] GEANT4 Collaboration, "GEANT4—a simulation toolkit", *Nucl. Instrum. Meth. A* **506** (2003) 250, doi:10.1016/S0168-9002(03)01368-8.

[68] R. Goldouzian et al., "Matching in $pp \to t\bar{t}W/Z/h + jet$ SMEFT studies", *JHEP* **06** (2021) 151, doi:10.1007/JHEP06(2021)151, arXiv:2012.06872.

[69] C. Degrande et al., "Automated one-loop computations in the standard model effective field theory", *Phys. Rev. D* **103** (2021) 096024, doi:10.1103/PhysRevD.103.096024, arXiv:2008.11743.

[70] CMS Collaboration, "Particle-flow reconstruction and global event description with the CMS detector", *JINST* **12** (2017) P10003, doi:10.1088/1748-0221/12/10/P10003, arXiv:1706.04965.

[71] CMS Collaboration, "Performance of missing transverse momentum reconstruction in proton-proton collisions at $\sqrt{s} = 13$ TeV using the CMS detector", *JINST* **14** (2019) P07004, doi:10.1088/1748-0221/14/07/P07004, arXiv:1903.06078.

[72] CMS Collaboration, "Technical proposal for the Phase-II upgrade of the Compact Muon Solenoid", CMS Technical Proposal CERN-LHCC-2015-010, CMS-TDR-15-02, 2015.

[73] CMS Collaboration, "Performance of electron reconstruction and selection with the CMS detector in proton-proton collisions at $\sqrt{s} = 8$ TeV", *JINST* **10** (2015) P06005, doi:10.1088/1748-0221/10/06/P06005, arXiv:1502.02701.

[74] CMS Collaboration, "Performance of the CMS muon detector and muon reconstruction with proton-proton collisions at $\sqrt{s} = 13$ TeV", *JINST* **13** (2018) P06015, doi:10.1088/1748-0221/13/06/P06015, arXiv:1804.04528.

[75] CMS Collaboration, "Search for supersymmetry in pp collisions at $\sqrt{s} = 13$ TeV in the single-lepton final state using the sum of masses of large-radius jets", *JHEP* **08** (2016) 122, doi:10.1007/JHEP08(2016)122, arXiv:1605.04608.

[76] M. Cacciari, G. P. Salam, and G. Soyez, "The anti-k_T jet clustering algorithm", *JHEP* **04** (2008) 063, doi:10.1088/1126-6708/2008/04/063, arXiv:0802.1189.

[77] M. Cacciari, G. P. Salam, and G. Soyez, "FastJet user manual", *Eur. Phys. J. C* **72** (2012) 1896, doi:10.1140/epjc/s10052-012-1896-2, arXiv:1111.6097.

[78] CMS Collaboration, "Pileup mitigation at CMS in 13 TeV data", *JINST* **15** (2020) P09018, doi:10.1088/1748-0221/15/09/p09018, arXiv:2003.00503.

[79] D. Bertolini, P. Harris, M. Low, and N. Tran, "Pileup per particle identification", *JHEP* **10** (2014) 059, doi:10.1007/JHEP10(2014)059, arXiv:1407.6013.

[80] M. Dasgupta, A. Fregoso, S. Marzani, and G. P. Salam, "Towards an understanding of jet substructure", *JHEP* **09** (2013) 029, doi:10.1007/JHEP09(2013)029, arXiv:1307.0007.

[81] A. J. Larkoski, S. Marzani, G. Soyez, and J. Thaler, "Soft drop", *JHEP* **05** (2014) 146, doi:10.1007/JHEP05(2014)146, arXiv:1402.2657.

[82] CMS Collaboration, "Identification of heavy, energetic, hadronically decaying particles using machine-learning techniques", *JINST* **15** (2020) P06005, doi:10.1088/1748-0221/15/06/P06005, arXiv:2004.08262.

[83] M. Cacciari and G. P. Salam, "Pileup subtraction using jet areas", *Phys. Lett. B* **659** (2008) 119, doi:10.1016/j.physletb.2007.09.077, arXiv:0707.1378.

[84] CMS Collaboration, "Jet energy scale and resolution in the CMS experiment in pp collisions at 8 TeV", *JINST* **12** (2017) P02014, doi:10.1088/1748-0221/12/02/P02014, arXiv:1607.03663.

[85] CMS Collaboration, "Identification of heavy-flavour jets with the CMS detector in pp collisions at 13 TeV", *JINST* **13** (2018) P05011, doi:10.1088/1748-0221/13/05/P05011, arXiv:1712.07158.

[86] J. G. Kreer, "A question of terminology", *IRE Trans. Inf. Theory* **3** (1957) 208, doi:10.1109/TIT.1957.1057418.

[87] C. E. Shannon, "A mathematical theory of communication", *Bell Syst. Tech. J.* **27** (1948) 379, doi:10.1002/j.1538-7305.1948.tb01338.x.

[88] ATLAS Collaboration, "Measurement of event shapes at large momentum transfer with the ATLAS detector in pp collisions at $\sqrt{s} = 7$ TeV", *Eur. Phys. J. C* **72** (2012) 2211, doi:10.1140/epjc/s10052-012-2211-y, arXiv:1206.2135.

[89] S. Ioffe and C. Szegedy, "Batch normalization: accelerating deep network training by reducing internal covariate shift", *Proc. Mach. Learn. Res.* **37** (2015) 448, arXiv:1502.03167.

[90] N. Srivastava et al., "Dropout: a simple way to prevent neural networks from overfitting", *J. Mach. Learn. Res.* **15** (2014) 1929.

[91] T.-Y. Lin et al., "Focal loss for dense object detection", *IEEE Trans. Pattern Anal. Mach. Intell.* **42** (2020) 318, doi:10.1109/TPAMI.2018.2858826, arXiv:1708.02002.

[92] R. J. Barlow and C. Beeston, "Fitting using finite Monte Carlo samples", *Comput. Phys. Commun.* **77** (1993) 219, doi:10.1016/0010-4655(93)90005-W.

[93] J. S. Conway, "Incorporating nuisance parameters in likelihoods for multisource spectra", in *PHYSTAT 2011*. 2011. arXiv:1103.0354. doi:10.5170/CERN-2011-006.115.

[94] J. Butterworth et al., "PDF4LHC recommendations for LHC run II", *J. Phys. G* **43** (2016) 023001, doi:10.1088/0954-3899/43/2/023001, arXiv:1510.03865.

[95] G. Ridolfi, M. Ubiali, and M. Zaro, "A fragmentation-based study of heavy quark production", *JHEP* **01** (2020) 196, doi:10.1007/JHEP01(2020)196, arXiv:1911.01975.

[96] CMS Collaboration, "First measurement of the cross section for top quark pair production with additional charm jets using dileptonic final states in pp collisions at $\sqrt{s} = 13$ TeV", *Phys. Lett. B* **820** (2021) 136565, doi:10.1016/j.physletb.2021.136565, arXiv:2012.09225.

[97] CMS Collaboration, "Measurement of the inelastic proton-proton cross section at $\sqrt{s} = 13$ TeV", *JHEP* **07** (2018) 161, doi:10.1007/JHEP07(2018)161, arXiv:1802.02613.

[98] ATLAS and CMS Collaborations, and LHC Higgs Combination Group, "Procedure for the LHC Higgs boson search combination in Summer 2011", Technical Report CMS-NOTE-2011-005, ATL-PHYS-PUB-2011-11, 2011.

[99] G. Cowan, K. Cranmer, E. Gross, and O. Vitells, "Asymptotic formulae for likelihood-based tests of new physics", *Eur. Phys. J. C* **71** (2011) 1554, doi:10.1140/epjc/s10052-011-1554-0, arXiv:1007.1727. [Erratum: doi:10.1140/epjc/s10052-013-2501-z].

[100] T. Junk, "Confidence level computation for combining searches with small statistics", *Nucl. Instrum. Meth. A* **434** (1999) 435, doi:10.1016/S0168-9002(99)00498-2, arXiv:hep-ex/9902006.

[101] A. L. Read, "Presentation of search results: The CL_s technique", *J. Phys. G* **28** (2002) 2693, doi:10.1088/0954-3899/28/10/313.

[102] CMS Collaboration, "Measurement and interpretation of differential cross sections for Higgs boson production at $\sqrt{s} = 13$ TeV", *Phys. Lett. B* **792** (2019) 369, doi:10.1016/j.physletb.2019.03.059, arXiv:1812.06504.

[103] CMS Collaboration, "Measurement of the cross section for $\mathrm{t\bar{t}}$ production with additional jets and b jets in pp collisions at $\sqrt{s} = 13$ TeV", *JHEP* **07** (2020) 125, doi:10.1007/JHEP07(2020)125, arXiv:2003.06467.

[104] CMS Collaboration, "Measurement of the $\mathrm{t\bar{t}b\bar{b}}$ production cross section in the all-jet final state in pp collisions at $\sqrt{s} = 13$ TeV", *Phys. Lett. B* **803** (2020) 135285, doi:10.1016/j.physletb.2020.135285, arXiv:1909.05306.

A Neural network input variables

Table A.1 lists the input variables of the DNN. The distributions of six of these input variables are shown in Fig. A.1.

Table A.1: Comprehensive list of the input variables of the DNN, which is described in Section 6. The "+" represents the relativistic four-momentum sum. Some variables are calculated for both the highest p_T (leading) and second-highest p_T (subleading) jet as indicated.

Name	Description
$t\bar{t}$ system	
b p_T	p_T of the leading (subleading) b jet
b score	DEEPCSV score of the leading (subleading) b jet
q p_T	p_T of the leading (subleading) non-b jet
q score	DEEPCSV score of the leading (subleading) non-b jet
$\Delta R(\mathrm{b},\mathrm{q})$	minimum ΔR between the leading (subleading) b jet and any non-b jet
$\Delta R(\mathrm{q},\mathrm{q})$	ΔR between the non-b jets closest and next-to-closest to the leading (subleading) b jet
$m(\mathrm{q}+\mathrm{q})$	invariant mass of the non-b jets closest and next-to-closest to the leading (subleading) b jet
$\Delta R(\mathrm{b},\mathrm{q}+\mathrm{q})$	ΔR between the leading (subleading) b jet and the sum of the nearest and next-to-nearest non-b jets
$m(\mathrm{b}+\mathrm{q}+\mathrm{q})$	invariant mass of the leading (subleading) b jet and the nearest and next-to-nearest non-b jets
$\Delta R(\mathrm{Z/H},\mathrm{b}+\mathrm{q}+\mathrm{q})$	ΔR between the Z or Higgs boson candidate and the sum of the leading (subleading) b jet and the non-b jets nearest and next-to-nearest to the leading (subleading) b jet
$\Delta R(\mathrm{Z/H},\mathrm{b}+\mathrm{b}+\mathrm{q}+\mathrm{q}+\ell)$	ΔR between the Z or Higgs boson candidate and the sum of the leading and subleading b jets, the non-b jets nearest and next-to-nearest to the leading (subleading) b jet, and the lepton
$m_T(\mathrm{b}+\ell,\vec{p}_T^{\,\mathrm{miss}})$	transverse mass of the subleading b jet and the lepton
$m(\mathrm{Z/H}+\mathrm{b})$	invariant mass of the Z or Higgs boson candidate and the nearest b jet
$m(\mathrm{b}+\mathrm{b})$	invariant mass of the leading and subleading b jets
$\Delta R(\mathrm{b},\mathrm{b})$	ΔR between the leading and subleading b jets
$\Delta R(\mathrm{Z/H},\mathrm{q})$	ΔR between the Z or Higgs boson candidate and the leading non-b jet
$\Delta R(\mathrm{Z/H},\mathrm{b})$	ΔR between the Z or Higgs boson candidate and the leading b jet
$\Delta R(\mathrm{Z/H},\ell)$	ΔR between the Z or Higgs boson candidate and the lepton
$m(\mathrm{Z/H}+\ell)$	invariant mass of the Z or Higgs boson candidate and the lepton
$\Delta R(\mathrm{b},\ell)$	ΔR between the leading (subleading) b jet and the lepton
$m(\mathrm{b}+\ell)$	invariant mass of the leading (subleading) b jet and the lepton
$N(\mathrm{b}_{\mathrm{out}})$	number of b jets outside the Z or Higgs boson candidate cone ($\Delta R > 0.8$)
$N(\mathrm{q}_{\mathrm{out}})$	number of non-b jets outside the Z or Higgs boson candidate cone ($\Delta R > 0.8$)
Event topology	
N(AK8 jets)	number of AK8 jets, including the Z or Higgs boson candidate
N(AK4 jets)	number of AK4 jets
N(Z/H)	number of AK8 jets with a minimum AK8 $\mathrm{b\bar{b}}$ tagger score of 0.8
AK8 m_{SD}	maximum m_{SD} of AK8 jets, excluding the Z or Higgs boson candidate
$H_T(\mathrm{b}_{\mathrm{out}})$	H_T of the b jets outside the Z or Higgs boson candidate cone ($\Delta R > 0.8$)
$H_T(\mathrm{b}_{\mathrm{out}},\mathrm{q}_{\mathrm{out}},\ell)$	H_T of all AK4 jets outside the Z or Higgs boson candidate cone ($\Delta R > 0.8$) and the lepton
sphericity	sphericity calculated from the AK4 jets and the lepton [88]
aplanarity	aplanarity calculated from the AK4 jets and the lepton [88]
Z or Higgs boson candidate substructure	
b_{in} score	maximum (minimum) DEEPCSV score of AK4 jets within the Z or Higgs boson candidate cone ($\Delta R < 0.8$)
$\Delta R(\mathrm{b}_{\mathrm{in}},\mathrm{b}_{\mathrm{out}})$	ΔR between one b jet within the Z or Higgs boson candidate cone ($\Delta R < 0.8$) and the leading b jet outside of the Z or Higgs boson candidate cone
$N(\mathrm{b}_{\mathrm{in}})$	number of b jets within the Z or Higgs boson candidate cone ($\Delta R < 0.8$)
$N(\mathrm{q}_{\mathrm{in}})$	number of non-b jets within the Z or Higgs boson candidate cone ($\Delta R < 0.8$)
Z/H $\mathrm{b\bar{b}}$ score	AK8 $\mathrm{b\bar{b}}$ tagger score of the Z or Higgs boson candidate

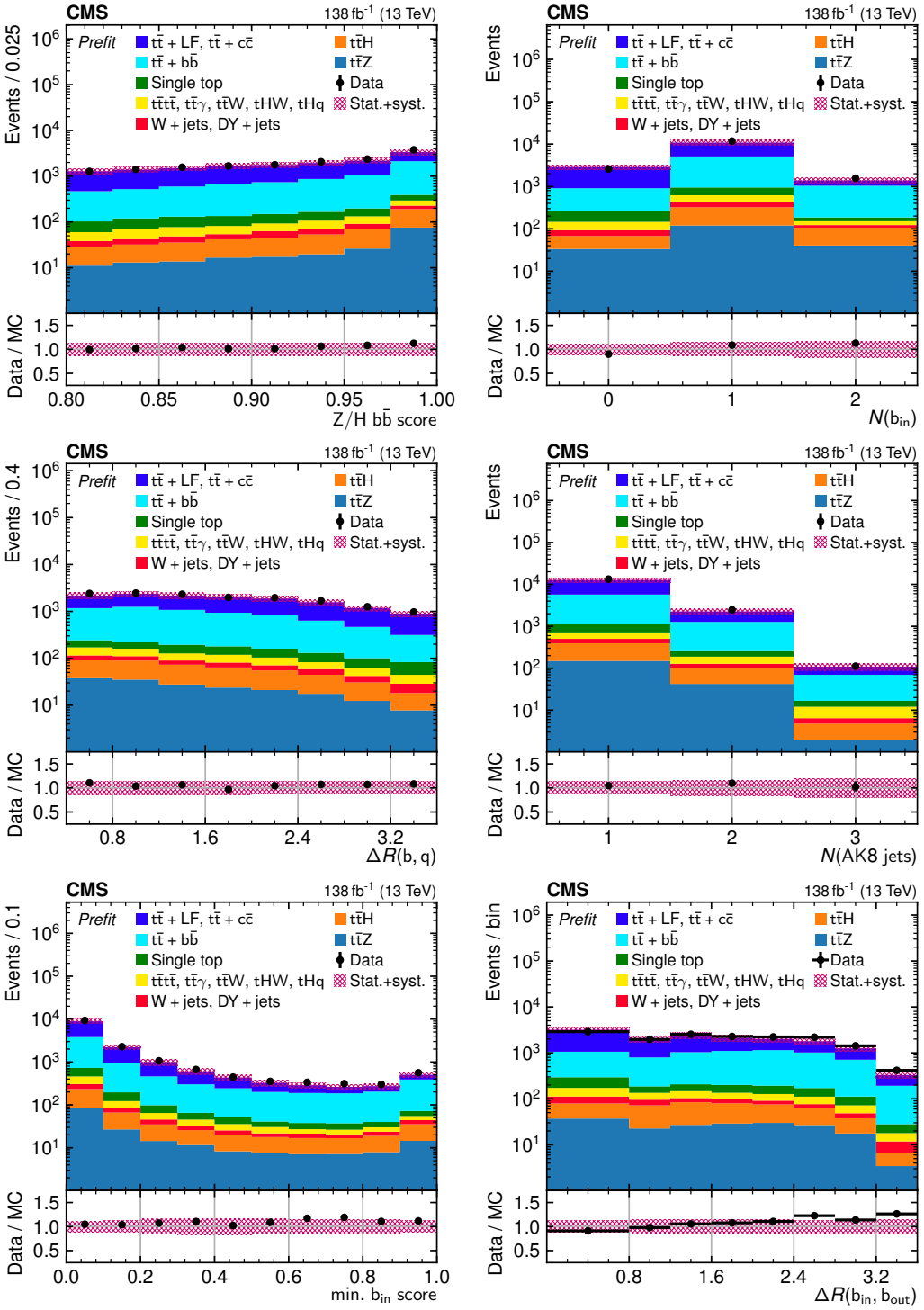

Figure A.1: Prefit expected (colored histograms) and observed (point) distributions of selected DNN input variables, each of which is described in detail in Table A.1. These distributions represent the combined 2016–2018 data-taking periods. The hatched bands represent the total statistical and systematic uncertainty in the expected distributions, while the vertical bars on the black points indicate the statistical uncertainty in the observed distributions and the horizontal bars indicate the bin widths. The lower panels show the ratio of the observed yields to the sum of the MC predictions.